Multi-scale computational homogenization of structured thin sheets

Coenen, E.W.C.

Award date:
2006

Multi-scale computational homogenization of structured thin sheets

E.W.C. Coenen
MT 06.48

Eindhoven University of Technology
Department of Mechanical Engineering
Division of Computational and Experimental Mechanics
TU/e Master Thesis Report
Supervisors / comittee:
dr.ir. V. Kouznetsova
prof.dr.ir M.G.D. Geers
dr.ir. W.A.M. Brekelmans
dr. T.J. Massart
dr.ir. I. Lopez
dr.ir. R.M.J. Voncken

December 8^{th} 2006, Eindhoven

Abstract

Structured and layered thin sheets are used in a variety of innovative applications, e.g. flexible displays, rollable solar cells or flexible electronics. Stacks of different materials, with often highly complex interconnects between layers, are thereby used which are typically loaded in bending combined with intrinsic thermo-mechanical mismatches. As a result different failure mechanisms at the level of the layered substructure occur, which constitute a serious reliability concern.

The development of these functional structures often calls for an analysis of the complex micro-macro structure-properties relations. The objective of this research is to develop a two-scale computational homogenization approach for structured thin sheets. This computational homogenization technique is essentially based on the solution of two nested boundary value problems, one for each scale. No closed-form constitutive model needs to be chosen for the macrolevel, which makes the technique suitable for dealing with complex loading and an evolving microstructure.

The three dimensional macroscopic structure is modelled as a shell-type boundary value problem derived from a classical shell theory. The shell theories used in this research are the Kirchhoff-Love and the kinematically more rich Mindlin-Reissner theories. The computational homogenization scheme can be imbedded in shell theory without any additional restrictions (with respect to the restrictions inherent to shell theory) to the macroscopic deformation. Large macroscopic displacements and rotations of the structure are possible.

The microstructure can be modelled and then solved as a standard boundary value problem. The different phases of the microstructure can be modelled with arbitrary constitutive models, e.g. non-linear or time-dependent. In this research a finite element method was used to solve the microscopic boundary value problem, but any other appropriate solution technique may be used as well.

The computational homogenization of structured thin sheets fits entirely in a standard shell mechanics framework. Generalized strains describing the local membrane strain, and curvature (and transverse shears for Mindlin-Reissner-sheets) are calculated for every material point and are used to formulate kinematic boundary conditions for the associated microstructural representative volume element (RVE). The three-dimensional RVE represents the full thickness and a periodic in-plane cell of the microstructure. The stress integration through the thickness of the shell is combined with an in-plane homogenization by averaging the resulting RVE stress field over the in-plane area of the microstructural cell after the solution of the microstructural boundary value problem. The hereby obtained generalized stress resultants are energy consistent with the definitions used in shell theories. As a result, the (numerical) generalized stress-strain relationship at every macroscopic point is readily available.

To illustrate the proposed framework, first the homogenized response of the a homogeneous RVE is compared to the generalized stress-strain response of the classical shell theories. Next,

the homogenized response of a heterogeneous microstructure for different prescribed macroscopic deformation modes is calculated. Two examples of multi-scale analyses are given, one for the transversely loaded sheet, and one for the sheet subjected to a twisting loading.

The developed multi-scale computational homogenization procedure is a useful and powerful tool for the analysis of structured thin sheets with any, possible complex, type of periodic microstructure.

Samenvatting

Dunne schalen bestaande uit lagen of een zekere microstructure worden gebuikt in vele innovative toepassingen, zoals flexible beeldschermen, oprolbare zonnencellen en flexibele elektronica. Een stapeling van verschillende materialen, met veelal zeer complexe verbindingen tussen de lagen, worden typisch belast door buiging vaak gecombineerd met belastingen resulterend uit verschillen in thermo-mechanische eigenschappen. Hierdoor ontstaan verschillende schade-mechanismen op het niveau van de gelaagde substructuur, welke een ernstige bedreiging voor de betrouwbaarheid zijn.

De ontwikkeling van deze functionele structuren vraagt vaak om een analyse van de complexe micro-macro gecombineerde mechanische eigenschappen. Het doel van dit onderzoek is het ontwikkelen van een twee-schalige numerieke homogenisatiemethode for dunne schalen bestaande uit een periodieke microstructuur. De numerieke homogenisatiemethode komt in feite neer op het oplossen van twee gekoppelde randwaardeproblemen, één op de macroscopische en één op de microscopische schaal. Er hoeft geen expliciet constitutief model gekozen te worden voor het beschrijven van het macroscopisch mechanisch gedrag. Hierdoor is de techniek geschikt voor gecompliceerde belastingspaden en houdt het rekening met veranderingen in de microstructuur.

De drie-dimensionele schaal wordt gemodelleerd door een schaalachtig randwaardeprobleem afgeleid van een klassieke schaaltheorie. De theorieën gebruikt in dit onderzoek zijn de Kirchhoff-Love en de kinematische rijkere Mindlin-Reissner theorieën. De numerieke homogenisatieschema's kunnen ingepast worden zonder extra restricties anders dan de restricties die samengaan met de klassieke schaaltheorieën. Grote macroscopisch verplaatsingen en rotaties zijn mogelijk.

The microstructuur kan gemodelleerd en opgelost worden als elk standaard randwaardeprobleem. De verschillende materialen in de microstructuur kunnen beschreven worden door elk willekeurig materiaalgedrag, bijvoorbeeld niet-lineair of tijdsafhankelijk. In dit onderzoek is de eindige elementen methode gebruikt voor het oplossen van het microscopisch randwaardeprobleem. Echter elke geschikte andere oplossingsmethode kan ook gebruikt worden.

Het numerieke homogenisatieschema voor schalen met een microstructuur past geheel binnen een standaard schaalmechanica-raamwerk. Gegeneraliseerde rekken, welke de lokale membraanrek en buiging (en voor MR-schalen afschuiving in de dwarsrichting) beschrijven, worden berekend voor ieder materieel macroscopisch punt. Deze worden vervolgens gebruikt om kinematische randvoorwaarden te formuleren voor een microstructureel representatief volume-element (RVE). Het drie-dimensionele RVE vertegenwoordigd de gehele dikte en een periodieke cel in het vlak van de macro-schaal. De integratie over de dikte en de homogenisatie in het vlak van de schaal, worden gecombineerd door het bepalen van een zeker gemiddelde van het RVE spanningsveld, nadat het microstructurele randwaardeprobleem is opgelost. Hierdoor worden de gegeneraliseerde rek-spanning relaties verkregen voor elk macroscopisch punt.

De verkregen gegeneraliseerde spanningresultanten zijn energie consistent met de definities gebruikt in de schaaltheorieën.

Om het voorgelegde raamwerk te illustreren, wordt allereerst het gehomogeniseerde gedrag van een RVE met homogene materiaaleigenschappen vergeleken met de gegeneraliseerde rekspanning relatie verkregen uit klassieke schaaltheorieën. Daarna is de gehomogeniseerde response van een heterogene microstructure voor verschillende voorgeschreven macroscopische vervormingsmodes berekend. Twee voorbeelden van de gekoppelde twee-schalige analyses zijn gegeven, een voor een schaal welke wordt belast in de dwarsrichting en een voor een schaal welke wordt belast door een wringende belasting.

Het gepresenteerde numerieke homogenisatie procedure is nuttig en krachtig voor de analyse van dunne schalen met een willekeurig, mogelijk zeer complex, type microstructuur.

Table of Contents

Notation

Vectors and tensors

The tensors and tensor products are used in a Cartesian coordinate system, with $\vec{e}_i$, $i = 1, 2, 3$ a set of unit base vectors. Summation convention is applied over repeated indices. The following notation is used throughout the report

Notation	Description
a	scalar
$\vec{a} = a_i \vec{e}_i$	vector
$\mathbf{A} = A_{ij} \vec{e}_i \vec{e}_j$	second-order tensor
${}^3\mathbf{A} = A_{ijk} \vec{e}_i \vec{e}_j \vec{e}_k$	third-order tensor
${}^n\mathbf{A} = A_{ijk\ldots n} \vec{e}_i \vec{e}_j \vec{e}_k \ldots \vec{e}_n$	n-order tensor

In this report vectors $\vec{a}$ are additively decomposed in an in-plane $\hat{\vec{a}}$ and transverse parts $\tilde{\vec{a}}$

$$\vec{a} = \hat{\vec{a}} + \tilde{\vec{a}} \qquad \text{with} \qquad \hat{\vec{a}} = \hat{\mathbf{I}} \cdot \vec{a} \qquad \text{and} \qquad \tilde{\vec{a}} = \tilde{\mathbf{I}} \cdot \vec{a} \tag{1}$$

where $\hat{\mathbf{I}} = \vec{e}_1 \vec{e}_1 + \vec{e}_2 \vec{e}_2$ is the in-plane unit tensor and $\tilde{\mathbf{I}} = \vec{e}_3 \vec{e}_3$ is the transverse unit tensor. Consistent with this definition also a second-order tensor $\mathbf{A}$ can be additively decomposed as

$$\mathbf{A} = \hat{\hat{A}} + \hat{\tilde{A}} + \tilde{\hat{A}} + \tilde{\tilde{A}} \tag{2}$$

Notation	Description
$\hat{\hat{A}} = A_{jk} \hat{\hat{I}}_{ij} \hat{\hat{I}}_{kl} \vec{e}_i \vec{e}_l$	in-plane to in-plane tensor
$\hat{\tilde{A}} = A_{jk} \hat{\tilde{I}}_{ij} \hat{\hat{I}}_{kl} \vec{e}_i \vec{e}_l$	in-plane to out-of-plane tensor
$\tilde{\hat{A}} = A_{jk} \tilde{\hat{I}}_{ij} \tilde{\hat{I}}_{kl} \vec{e}_i \vec{e}_l$	out-of-plane to in-plane tensor
$\tilde{\tilde{A}} = A_{jk} \tilde{\tilde{I}}_{ij} \tilde{\tilde{I}}_{kl} \vec{e}_i \vec{e}_l$	out-of-plane to out-of-plane tensor

The following operations are used

Operation	Description
$\vec{a}\vec{b} = a_i b_j \vec{e}_i \vec{e}_j$	dyadic product
$\mathbf{A} \cdot \mathbf{B} = A_{ij} B_{jk} \vec{e}_i \vec{e}_k$	inner product
$\mathbf{A} : \mathbf{B} = a_{ij} b_{ji}$	double inner product
∂	partial derivative
$\nabla \vec{a} = \nabla_i a_j \vec{e}_i \vec{e}_j$	gradient operator
$\nabla \cdot \vec{a} = \nabla_i a_i$	divergence operator
$\mathbf{A}^c$, $A^c_{ij} = A_{ji}$	conjugate of a second-order tensor
${}^3\mathbf{A}^{LC}$, $A^{LC}_{ijk} = A_{jik}$	left conjugate of a third-order tensor
${}^3\mathbf{A}^{RC}$, $A^{RC}_{ijk} = A_{ikj}$	right conjugate of a third-order tensor
$\mathbf{A}^{-1}$	inverse
δ	variation
$\det(\mathbf{A})$	determinant

Matrices and Columns

The matrix and column notation used throughout this work is

Notation	Description
a	scalar
$\underline{a}$	column
$\underline{\underline{A}}$	matrix
Operation	**Description**
$\underline{\underline{A}}^{-1}$	inverse
$\underline{\underline{A}}^T$	transpose
$\underline{\underline{A}}\,\underline{\underline{B}}$	matrix product

Chapter 1

Introduction

Structured and layered thin sheets are used in a variety of innovative applications, e.g. flexible displays, rollable solar cells or flexible electronics. Stacks of different materials, with often highly complex interconnects between layers, are thereby used which are typically loaded in bending combined with intrinsic thermo-mechanical mismatches. As a result, different failure mechanisms at the level of the layered substructure occur, which constitutes a serious reliability concern.

For the design of these structured and heterogeneous systems the observed overall macroscopic behaviour is important. In many cases, the loading is cyclic and mechanical fatigue effects arise, originating from evolving microstructural morphology and properties. Consequently, the behaviour of the microstructure and its influence on the macroscopic response needs to be taken into account.

Direct computational simulations of the structured thin sheets are very expensive, when modelling the heterogeneities in detail. Also, modelling thin structures with continuum elements often leads to high aspect ratios, which degrades the conditioning of the equations and the accuracy of the solution [1]. Therefore, the analysis of structured thin sheets is mostly performed in terms of effective properties combined with shell theories. The effective stress-strain material behaviour can be obtained by experimental methods. Extensive testing of sheet samples with different microstructures subjected to various deformation modes and loading paths, is very expensive and may be avoided by determining the effective properties by means of analytical or numerical homogenization techniques.

The homogenization theory is based on the asymptotic expansion method, which assumes the ratio of the characteristic dimensions of the heterogeneities and the macrostructure to approach zero. For structured sheets this ratio applies to the in-plane dimensions. The ratio of the thickness of the sheet and its in-plane dimensions also should tend to zero for shell theories to apply. It was shown in the work of Buannic and Cartraud[2] that different effective stiffnesses can be obtained depending on the order in which the two ratios approach zero relative to each other.

The effective properties of materials with a complex evolving microstructure can be determined by a computational homogenization methods using the concept of a representative volume element (RVE). These so-called unit cell methods serve a twofold purpose: they provide valuable information on the local microstructural fields as well as the effective material properties. The unit cell methods take benefit from the assumption of local periodicity exhibited by the microstructure. The microstructure can have different morphologies corresponding

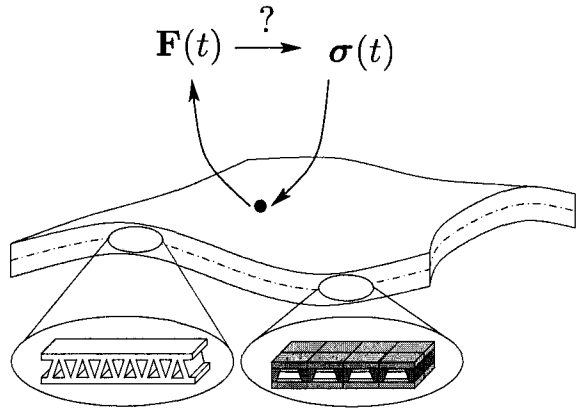

Figure 1.1: Example structured thin sheet.

to different macroscopic points [5]. The concept of local periodicity is schematically illustrated in Figure 1.1.

When the unit cell-method is used within a multi-scale computational homogenization analysis, the modelling procedures do not lead to closed-form overall constitutive equations. The stress-strain relationship is computed at every point of interest of the macroscopic structure by detailed modelling of the microstructure attributed to that point as schematically shown in Figure 1.1. Such a multi-scale approach [5] *a*) does not require any constitutive assumption on the macrolevel; *b*) enables the incorporation of large deformations and rotations on both micro and macrolevels; *c*) is suitable for arbitrary material behaviour, including physically non-linear and time-dependent response; *d*) provides the possibility to introduce detailed microstructural information, including the physical and geometrical evolution of the microstructure into the macroscopic analysis and *e*) allows the use of any modelling technique on the microlevel, e.g. the finite element method.

Computational homogenization theory appears to be a powerfull method, since it can be applied to a microstructure of general shape, and arbitrary heterogeneity. But, the "classical", here called "first-order", computational homogenization techniques are built entirely within a standard local continuum mechanics concept, where the response at a (macroscopic) material point is taken to depend on the deformation (i.e. the first gradient of the displacement field) history at that point only [6]. In general, the upscaling of the deformation of structured thin sheets towards a shell-type continuum is second-order in nature. Therefore, only certain types of structured thin sheets, e.g. some composite and sandwich sheets, can be homogenized by using first-order computational homogenization layerwise. The through-thickness domain of the sheet is in this case assumed to consist of several independent (homogenized) layers. The effective material properties of the layers can be determined by first-order computational homogenization techniques and the shell-structure can then be analyzed by application of an appropriate composite shell theory [4].

For example, a homogenization technique for sandwich structures has been presented in [10, 8]. Here the core section of the structure was modelled with continuum elements with the constitutive behaviour obtained by classical homogenization of the core, whereas beam elements were used to model the face sheets. When it is assumed that the face sheets carry the in-plane loads and bending moments, while the core has to keep the face sheets at the desired

distance and carries the transverse shear loads, the core is subjected to only simple first-order deformation modes and a first-order homogenization technique is sufficient to determine the effective properties of the core.

For a shell with an arbitrary (in-plane periodic) microstructure, the reduction to a stack of independent homogeneous layers, is not appropriate. Both the first-order (membrane strain, and transverse shear) and second-order (bending) through-thickness effective properties need to be taken into account. This has been done for the homogenization of a periodic beam-like structures in [3], where the elastic properties of the beam were determined. The obtained effective properties only apply to small deformation and simple-loading path, also the evolution of the microstructure can not be taken into account.

The methodology used in this master project relies on a second-order computational homogenization procedure, which is suitable for multi-scale modelling presented previously in [5] for a second-gradient continuum. It has the advantages of a multi-scale analyses as discussed above, because it solves the boundary value problems at the microlevel and the macrolevel simultaneously. The actual three-dimensional heterogeneous sheet is represented by a homogenized shell with the homogenized high-order properties obtained from the analysis of a microstructural RVE, which represents the full thickness and a periodic in-plane cell of the macroscopic structure (e.g. a single pixel in a flexible display).

In Chapter 2 two shell type formulations used at the macrolevel are summarized. The macro-sheet is represented by Kirchhoff-Love and the kinematically more rich Mindlin-Reissner (with transverse shear) shell elements. The quasi-static equilibrium equations are formulated, which state that the forces and moments acting on a through-thickness fiber of a shell should be in equilibrium.

The vicinity of such a through-thickness fiber is represented by the microstructural RVE for which details on the microscopic boundary value problem are given Chapter 3. At the small RVE scale all microstructural constituents are treated as an ordinary continuum, described by standard first-order equilibrium and constitutive equations. The microscopic boundary value problem is completed by essential and natural boundary conditions derived for the homogenization towards Kirchhoff-Love and Mindlin-Reissner shell types. The obtained micro-scale stress state is homogenized towards a three-dimensional macroscopic shell structure, the relations for the determination of the overall macroscopic stress resultants are elaborated.

The microstructural boundary value problem is solved by the finite element (FE) method. The implementation and the solution approach are described in Section 4.1. The macroscopic stress measures are extracted from the FE solution and macroscopic consistent tangents are obtained by a condensation of the total microstructural stiffness. This is outlined in Section 4.2.

In Chapter 5 properties of the homogenized microstructural response are discussed and two example of the coupled numerical analysis are given. Chapter 6 gives a summary of the conclusions and recommendations on the practical use of the computational homogenizing technique for structured thin sheets.

Chapter 2

Macro mechanics of a shell-type structure

The mechanical system considered at the macrolevel is a shell. Depending on the structural assumptions made, different shell theories can be derived. In this chapter, the kinematics of thin sheets is described using assumptions of two most widely used shell theories. The shell equilibrium equations based on the stress and couple-stress resultants are derived.

Within the multiscale computational homogenization framework, the shell problem considered at the macrolevel belongs to the class of large deformation problems. In general the displacements can be large, therefore an "in-plane" updated Lagrange approach combined with the co-rotational formulation will be used. The membrane strains can be large while the radius of curvature and the transverse shear strains need to be small to comply with the assumptions of standard shell theories as will be shown in this chapter.

The boundary value problem at the microscale makes use of a total Lagrange approach. Therefore a strain pull-back and stress push-forward is necessary to account for the different reference configurations used at the micro- and macro-scales.

2.1 Shell theories

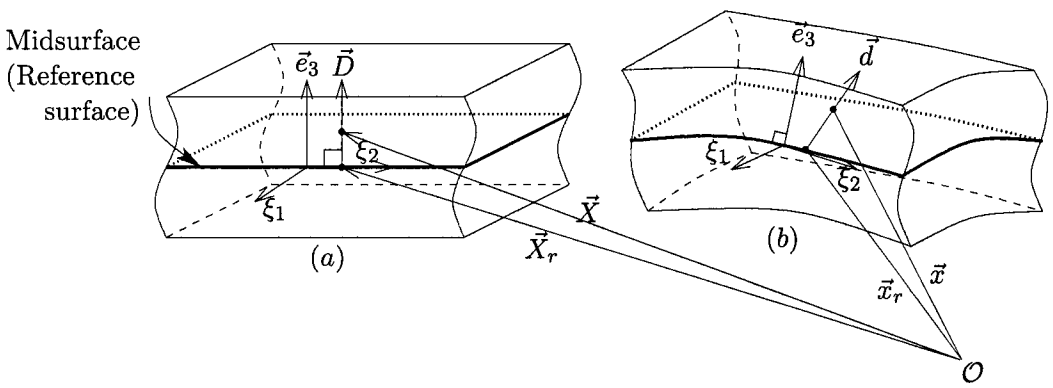

Figure 2.1: Position vectors with respect to the global coordinate system at points within the shell in the reference (a) and current (b) configurations.

A shell belongs to the class of structural elements and the term applies to a thin body bounded by two curved surfaces. In shell theory a smooth surface, called the reference surface, is introduced. The reference surface is parameterized by two material curvilinear coordinates ξ_α, $\alpha = 1, 2$. A material point on the reference surface in the undeformed reference configuration is described by the position vector $\vec{X}_r(\xi_\alpha)$ and in the current deformed configuration by $\vec{x}_r(\xi_\alpha)$, see Figure 2.1. For a sufficiently large radius of curvature in the reference configuration, any point in the shell body is uniquely identified in the undeformed configuration according to its reference position

$$\vec{X}(\xi_\alpha, \zeta) = \vec{X}_r(\xi_\alpha) + \zeta \vec{D}(\xi_\alpha) \tag{2.1}$$

where $\vec{D}$ is the unit normal to the undeformed reference surface, also called the initial director, and ζ is the material coordinate describing the distance between a point and its corresponding point on the reference surface. Material lines, in the reference configuration oriented along the initial director $\vec{D}$, are called fibers. The thickness h of a shell is defined as the distance between the bottom and the top surfaces along the fiber. The initial local thickness of the shell is denoted H. Each surface of constant ζ is called lamina. The reference surface is the lamina that corresponds to $\zeta = 0$. In this work the reference surface is chosen to be midway between the top and bottom surfaces and therefore it will be called midsurface.

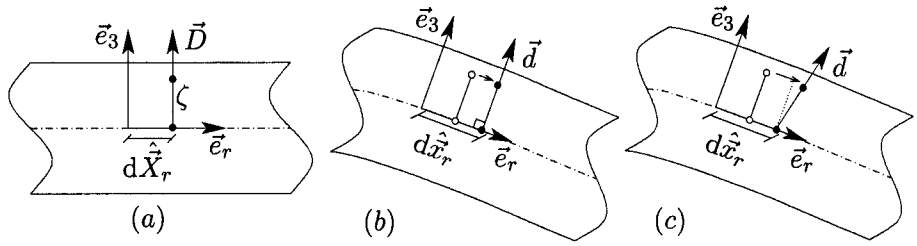

Figure 2.2: Reference configuration of a shell (a) and the deformed configuration of a Kirchhoff-Love (b) and Mindlin-Reissner (c) type shell.

The key feature that distinguishes shells from continua is that certain assumptions are made with respect to the kinematics and the state of stress. The major kinematical assumption concerns the deformation of the fibers. Two types of shell theory are widely used: Kirchhoff-Love (KL) shell theory and Mindlin-Reissner (MR) shell theory. In the KL theory the fibers are assumed to remain straight and normal to the midsurface, see Figure 2.2b. In the MR theory the fibers are also assumed to remain straight, but not necessarily normal to the midsurface, thereby admitting transverse shear [1], see Figure 2.2c. Taking into account that the fibers are assumed rigid, the position vector of a material point in the deformed configuration is written as

$$\vec{x}(\xi_\alpha, \zeta) = \vec{x}_r(\xi_\alpha) + \zeta \vec{d}(\xi_\alpha) \tag{2.2}$$

where $\vec{d}$ is vector along a fiber in the current configuration, called current director.

2.2 Displacement and strains

The local deformation of a shell is described using the local co-rotational basis $\{\vec{e}_1, \vec{e}_2, \vec{e}_3\}$. This coordinate system in general varies from point to point and it is constructed in such a

way that the plane $(\vec{e}_1, \vec{e}_2)$ is always tangent to the current midsurface. The $\vec{e}_3$-direction is the local normal to the current midsurface. Initially, $\vec{e}_3$ coincides with the director $\vec{D}$.

In the reference configuration, the position of a material point at the infinitesimal distance from the local basis origin can be written as a superposition of its corresponding position on the midsurface $d\vec{X}_r$ and a distance ζ along the rigid fiber

$$\mathrm{d}\vec{X} = \mathrm{d}\vec{X}_r + \zeta\vec{D} = \mathrm{d}\hat{\vec{X}} + \zeta\vec{D} \tag{2.3}$$

In the current configuration the position of this material point is then written as

$$\mathrm{d}\vec{x} = \mathrm{d}\vec{x}_r + \zeta\vec{d} \tag{2.4}$$

with $\mathrm{d}\vec{x}_r$ the position on the midsurface in the current configuration. In this report vectors $\vec{a}$ are splitted into an in-plane part $\hat{\vec{a}}$ and a transverse part $\tilde{\vec{a}}$. The in-plane part of the position vector of the midplane $\mathrm{d}\hat{\vec{x}}_r$ and the in-plane part of the director $\hat{\vec{d}}$ are described by "generalized" strains. KL shells use the generalized strain tensors $\boldsymbol{\mathcal{E}}_0$ and $\boldsymbol{\mathcal{K}}_0$ called the membrane strain and the curvature tensor, respectively. In addition to these two generalized strains, the MR shell has a transverse shear strain $\hat{\vec{\gamma}}_0$, which describes the rotation of the fiber with respect to the midsurface. Because of the shell assumptions, the midsurface position vector $\vec{x}_r$ and the director $\vec{d}$ depend only on two parameters (here the in-plane coordinates X_1 and X_2) their gradient is fully determined by the in-plane gradient operator

$$\hat{\nabla}_0 = \frac{\partial}{\partial X_1}\vec{e}_1 + \frac{\partial}{\partial X_2}\vec{e}_2 \tag{2.5}$$

The generalized strain tensors are defined as

$$\hat{\hat{\mathbf{I}}} + \boldsymbol{\mathcal{E}}_0 = (\hat{\nabla}_0\hat{\vec{x}}_r)^c, \qquad \boldsymbol{\mathcal{K}}_0 = (\hat{\nabla}_0\hat{\vec{d}})^c, \qquad \text{and} \qquad \hat{\vec{\gamma}}_0 = \hat{\vec{d}} \tag{2.6}$$

where $\hat{\hat{\mathbf{I}}}$ is the in-plane unit tensor. Note that the tensors $\boldsymbol{\mathcal{E}}_0$ and $\boldsymbol{\mathcal{K}}_0$ and the vector $\hat{\vec{\gamma}}_0$ have only the in-plane components. The subscript "0" refers to the undeformed reference configuration. Using these generalized strain definitions the material line element in the undeformed reference configuration (2.3) can be mapped to the in-plane part of this material line element in the current configuration $\mathrm{d}\hat{\vec{x}}$ as

$$\mathrm{d}\hat{\vec{x}} = (\hat{\hat{\mathbf{I}}} + \boldsymbol{\mathcal{E}}_0 + \zeta\boldsymbol{\mathcal{K}}_0) \cdot \mathrm{d}\hat{\vec{X}} + \zeta\hat{\vec{\gamma}}_0, \tag{2.7}$$

In KL-theory, the transverse shear is assumed to be zero and the last term of equation (2.7) vanishes. The combined tensor

$$\hat{\hat{\mathbf{F}}}_{\mathcal{L}} = (\hat{\hat{\mathbf{I}}} + \boldsymbol{\mathcal{E}}_0 + \zeta\boldsymbol{\mathcal{K}}_0) \tag{2.8}$$

can be consider as a two dimensional in-plane deformation gradient tensor describing the deformation of an infinitesimal line element within a lamina. The in-plane displacement of the director uses an infinitesimal rotation description, therefore transverse shear strains and the radius of curvature are limited, i.e. $\hat{\vec{\gamma}}_0 \ll 1$ and $H\kappa_0 \ll 1$. Here κ_0 is the local maximum radius of curvature. The latter condition $H\kappa_0 \ll 1$, is an important requirement for the application of shell theories. When it is not met, the classical shell theory is not applicable [1].

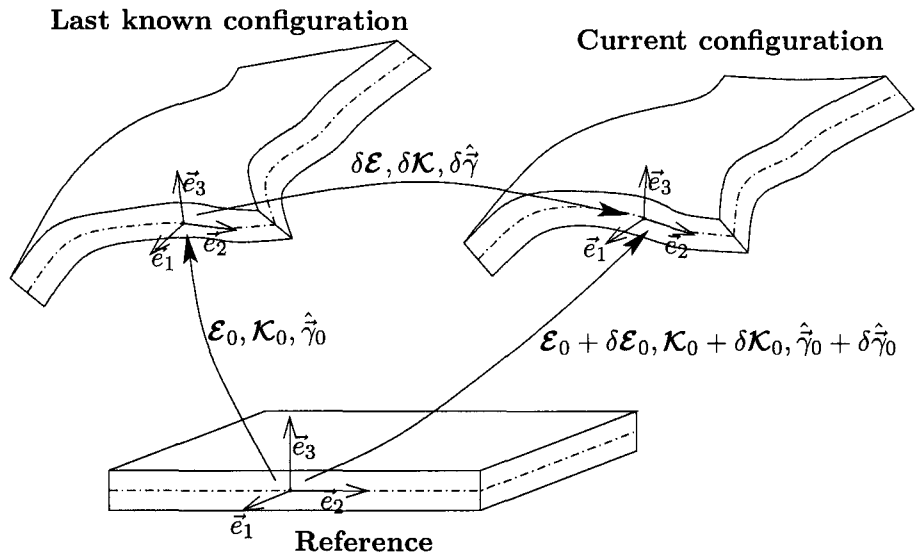

Figure 2.3: The total and updated Lagrange approach.

The transverse part $\mathrm{d}\tilde{\vec{x}}$ of the material line element (2.3) may also be described by the generalized strains. The transverse displacement vector $\mathrm{d}\tilde{\vec{u}} = \mathrm{d}\tilde{\vec{x}} - \mathrm{d}\tilde{\vec{X}}$ is written as

$$\mathrm{d}\tilde{\vec{u}} = \vec{e}_3\hat{\vec{\gamma}}_0^r \cdot \mathrm{d}\hat{\vec{X}} - \frac{1}{2}\vec{e}_3\boldsymbol{\mathcal{K}}_0 : \mathrm{d}\hat{\vec{X}}\mathrm{d}\hat{\vec{X}}. \tag{2.9}$$

where $\hat{\vec{\gamma}}_0^r = \hat{\nabla}_0\tilde{\vec{x}}_r \cdot \vec{e}_3 = \hat{\vec{0}}$. In shell theories it is usually assumed that the midsurface (and thus also the laminas) remains tangent to the plane $(\vec{e}_1, \vec{e}_2)$, therefore typically $\hat{\vec{\gamma}}_0^r = \hat{\vec{0}}$, however it is included here and in following for the sake of generality and ease of some derivations. The transverse displacement vector will be of special importance in the MR shell-type, since the related generalized stresses counterbalances the transverse shear.

Furthermore, for the forthcoming derivations it is convenient to write the deformation gradient tensor of the midsurface as

$$\mathbf{F} = (\hat{\hat{\mathbf{I}}} + \boldsymbol{\mathcal{E}}_0) + \hat{\vec{\gamma}}_0\vec{e}_3 + \vec{e}_3\hat{\vec{\gamma}}_0^r + \frac{\mathrm{d}h}{\mathrm{d}H}\vec{e}_3\vec{e}_3 \tag{2.10}$$

Note, that when the shell theories are taken into account, i.e. $h = H$ and $\hat{\vec{\gamma}}_0^r = \hat{\vec{0}}$ then (2.10) simplifies to

$$\mathbf{F} = (\hat{\hat{\mathbf{I}}} + \boldsymbol{\mathcal{E}}_0) + \hat{\vec{\gamma}}_0\vec{e}_3 + \vec{e}_3\vec{e}_3 \tag{2.11}$$

2.3 Numerical implementation: Updated Lagrange

The engineering generalized strains $\boldsymbol{\mathcal{E}}_0$, $\boldsymbol{\mathcal{K}}_0$, and $\hat{\vec{\gamma}}_0$ are defined with respect to the undeformed reference configuration, see Figure 2.3. In the computational homogenization framework an updated Lagrange approach will be used for the finite element solution procedure at the macrolevel. Therefore, the generalized strains need to be rewritten with respect to the current

configuration. The in-plane gradient operators of the current and reference configuration are related by $\hat{\nabla}(\zeta) = \hat{\mathbf{F}}_{\mathcal{L}}^{-c}(\zeta) \cdot \hat{\nabla}_0$. Because $\boldsymbol{\mathcal{E}}_0$ and $\boldsymbol{\mathcal{K}}_0$ are defined with respect to the reference surface, only the in-plane gradient operators at the reference surface is needed for the push-forward of the strains. So, the current in-plane gradient operator at the reference surface $\hat{\nabla}$ can be written as the push-forward

$$\hat{\nabla} = (\hat{\hat{\mathbf{I}}} + \boldsymbol{\mathcal{E}}_0)^{-c} \cdot \hat{\nabla}_0 \tag{2.12}$$

The configuration update is only an in-plane update, since the thickness changes are not taken into account in the shell theory. Substitution of (2.12) in the definitions of the generalized strains (2.6) expressed as gradient of variation of the vectors and taking into account that there is no update in the transverse direction, gives

$$\delta\boldsymbol{\mathcal{E}}_0 = (\hat{\nabla}\delta\hat{\vec{x}}_r)^c \cdot (\hat{\hat{\mathbf{I}}} + \boldsymbol{\mathcal{E}}_0) = \delta\boldsymbol{\mathcal{E}} \cdot (\hat{\hat{\mathbf{I}}} + \boldsymbol{\mathcal{E}}_0) \tag{2.13}$$

$$\delta\boldsymbol{\mathcal{K}}_0 = (\hat{\nabla}\delta\hat{\vec{d}})^c \cdot (\hat{\hat{\mathbf{I}}} + \boldsymbol{\mathcal{E}}_0) = \delta\boldsymbol{\mathcal{K}} \cdot (\hat{\hat{\mathbf{I}}} + \boldsymbol{\mathcal{E}}_0) \tag{2.14}$$

$$\delta\hat{\vec{\gamma}}_0 = \delta\hat{\vec{\gamma}}. \tag{2.15}$$

These relations define the true generalized strain increments as

$$\delta\boldsymbol{\mathcal{E}} = (\hat{\nabla}\delta\hat{\vec{x}}_r)^c, \qquad \delta\boldsymbol{\mathcal{K}} = (\hat{\nabla}\delta\hat{\vec{d}})^c, \qquad \text{and} \qquad \delta\hat{\vec{\gamma}} = \delta\hat{\vec{d}} \tag{2.16}$$

The incremental true strain tensors $\delta\boldsymbol{\mathcal{E}}$ and $\delta\boldsymbol{\mathcal{K}}$, may be compared to be rate of deformation tensors.

2.4 The generalized stress resultants

In the case of plane stress, the stress components in the thickness direction vanish. In shell theory, the stress component along a fiber is assumed to be zero. The generalized stress resultants used in shell theories are calculated from the in-plane $\hat{\boldsymbol{\sigma}}$ and the transverse shear $\tilde{\boldsymbol{\sigma}}$ parts of the Cauchy stress tensor. The true stress resultant $\mathbf{N}$ is defined as

$$\mathbf{N} = \int_h \hat{\boldsymbol{\sigma}} \mathrm{d}h \tag{2.17}$$

where $\mathbf{N}$ represents the resulting force per unit length working on a line in the midsurface in the current configuration. Considering the balance of forces on such a line leads to the requirement that the in-plane divergence of the stress resultant tensor is zero [1]

$$\hat{\nabla} \cdot \mathbf{N} = \hat{\vec{0}} \tag{2.18}$$

The moment per unit length working on a line in the midsurface in the current configuration is given by the true couple-stress resultant tensor $\mathbf{M}$. When making use of the assumption that the fibers are inextensible the true couple-stress resultant is defined as

$$\mathbf{M} = \int_h \zeta\hat{\boldsymbol{\sigma}} \mathrm{d}h \tag{2.19}$$

In the Mindlin-Reissner shell-type also a true transverse shear resultant along a fiber is defined

$$\hat{Q} = \vec{e}_3 \cdot \int_h \tilde{\boldsymbol{\sigma}} \mathrm{d}h \tag{2.20}$$

Considering the equilibrium of moments on a line in the midsurface the following balance equation can be derived

$$\hat{\nabla} \cdot \mathbf{M} - \hat{\vec{Q}} = \hat{\vec{0}} \tag{2.21}$$

In KL-shells the transverse shear is zero, requiring a constant moment for bending [1]

For the finite element solution of the boundary value problem at the microlevel a total Lagrange formulation is used therefore, a relation between the true stress resultants and the engineering stress resultants need to be established. The virtual work performed on a fiber in the current configuration (i.e. the virtual work per unit of current midsurface area) by virtual displacement is written using the incremental true generalized strains as

$$\delta W = \left(\int_h \hat{\boldsymbol{\sigma}} \mathrm{d}h \right) : \delta \boldsymbol{\mathcal{E}}^c + \left(\int_h \zeta \hat{\boldsymbol{\sigma}} \mathrm{d}h \right) : \delta \boldsymbol{\mathcal{K}}^c + \left(\vec{e}_3 \cdot \int_h \tilde{\hat{\boldsymbol{\sigma}}} \mathrm{d}h \right) \cdot \delta \hat{\vec{\gamma}} \tag{2.22}$$

By definition the first Piola-Kirchhoff stress tensor $\mathbf{P}$ is related to the Cauchy stress tensor $\boldsymbol{\sigma}$ by the deformation gradient tensor $\mathbf{F}$ as

$$\mathbf{P} = \det(\mathbf{F}) \boldsymbol{\sigma} \cdot \mathbf{F}^{-c} \tag{2.23}$$

It can be shown that when it is assumed that the stress component along a fiber is zero and when γ_0 is small, the pull-back of the in-plane stress components can be written as

$$\hat{\hat{\mathbf{P}}} = \det(\hat{\hat{\mathbf{I}}} + \boldsymbol{\mathcal{E}}_0) \hat{\boldsymbol{\sigma}} \cdot (\hat{\hat{\mathbf{I}}} + \boldsymbol{\mathcal{E}}_0)^{-c} \tag{2.24}$$

and the pull-back of the transverse shear components is here defined by

$$\tilde{\hat{\mathbf{P}}} = \det(\mathbf{F}) \tilde{\hat{\boldsymbol{\sigma}}} \tag{2.25}$$

Substituting these pull-back relations in equation (2.22), taking into account the relations between the increments of the engineering and true strains (2.13)-(2.15), and considering that $\mathrm{d}h = \mathrm{d}H$, the virtual work is written as

$$\delta W = \frac{1}{\hat{J}} \left\{ \left(\int_H \hat{\hat{\mathbf{P}}} \mathrm{d}H \right) : \delta \boldsymbol{\mathcal{E}}_0^c + \left(\int_H \zeta \hat{\hat{\mathbf{P}}} \mathrm{d}H \right) : \delta \boldsymbol{\mathcal{K}}_0^c + \left(\vec{e}_3 \cdot \int_H \tilde{\hat{\mathbf{P}}} \mathrm{d}H \right) \cdot \delta \hat{\vec{\gamma}}_0 \right\} \tag{2.26}$$

with $\hat{J} = \det(\hat{\hat{\mathbf{I}}} + \boldsymbol{\mathcal{E}}_0)$ and $\hat{\hat{\mathbf{P}}}$ the in-plane components and $\tilde{\hat{\mathbf{P}}}$ the transverse traction components of the first Piola-Kirchhoff stress tensor. The stress, couple-stress and transverse shear resultants with respect to the reference configuration are now defined as

$$\mathbf{N}_0 = \int_H \hat{\hat{\mathbf{P}}} \mathrm{d}H = \hat{J} \mathbf{N} \cdot (\boldsymbol{\mathcal{E}}_0 + \hat{\hat{\mathbf{I}}})^{-c} \tag{2.27}$$

$$\mathbf{M}_0 = \int_H \zeta \hat{\hat{\mathbf{P}}} \mathrm{d}H = \hat{J} \mathbf{M} \cdot (\boldsymbol{\mathcal{E}}_0 + \hat{\hat{\mathbf{I}}})^{-c} \tag{2.28}$$

$$\hat{\vec{Q}}_0 = \vec{e}_3 \cdot \int_H \tilde{\hat{\mathbf{P}}} \mathrm{d}H = \hat{J} \hat{\vec{Q}}. \tag{2.29}$$

2.5 Inconsistencies of shell theories

The assumptions of the shell theories introduce several inconsistencies. For example, the stress component along a fiber is assumed zero, inextensibility of the fibers, however, contradicts this assumption. Furthermore, a constant shear strain in the transverse direction supposes a constant shear stress through the thickness of the shell. However, unless a shear traction is applied to the top or bottom surfaces, the transverse shear must vanish at these surfaces. Therefore, in general a constant shear stress and corresponding straight fibers are not possible. Omitting the transverse shear in KL shell theory, requires the moment to be constant as can be seen from the moment equilibrium equation. In general, the moment is not constant and the assumption of zero transverse shear contradicts the equilibrium equation.

Also, traction in the direction of the fibers applied to either surface of the shell are inconsistent with the assumption that the stress component along a fiber is zero. Obviously, the stress component must equal the applied traction. However, this is neglected in structural theories because this stress component is much smaller than the in-plane stresses; only a small fraction of the energy is absorbed by these stresses and it has little effect on the deformation [1].

These contradictions will be reconciled in the macro-micro transition described in chapter 3, where the constitutive relation between the macrostructural engineering generalized strains and the stress resultants, will be provided by the homogenization of the mechanical response of a microstructural RVE.

Chapter 3

Computational homogenization of shell-type continua

The two-scale homogenization scheme is based on the solution of two nested boundary value problems, one for the macroscopic and one for the microscopic scales. A scheme of the computational homogenization towards a shell continuum is presented in Figure 3.1. In the homogenization of structured thin sheets, the generalized strains $\boldsymbol{\mathcal{E}}_0$, $\boldsymbol{\mathcal{K}}_0$ (and $\hat{\vec{\gamma}}_0$) are calculated for every material point of the macrostructure (e.g. the integration points of the macroscopic mesh within a finite element environment).

The generalized strains are used to prescribe kinematical boundary conditions on the microstructural RVE. The microscale boundary value problem will be described in more detail in Section 3.1 and the kinematical boundary conditions for the KL and the MR shell-types are derived in Sections 3.2.1 and 3.3.1, respectively. The microscopic inconsistencies are reconciled by no longer assuming the fibers to be rigid. This is of special importance for the MR shell-type.

After the solution of the RVE boundary value problem (which will be summarized in Section 4.1), the obtained microscale stress state is homogenized. The macroscopic stress resultants $\mathbf{N}_0$, $\mathbf{M}_0$ (and $\hat{\vec{Q}}_0$) are derived exploiting the Hill-Mandel energy condition.

3.1 Microscopic boundary value problem

The problem at the microstructural (RVE) level is formulated as a standard problem in quasi-static continuum solid mechanics. In the absence of body forces the equilibrium equation for the microstructural RVE in terms of the first Piola-Kirchhoff stress tensor $\mathbf{P}_\mathrm{m}$ (related to the Cauchy stress tensor by $\mathbf{P}_\mathrm{m} = \det(\mathbf{F}_\mathrm{m})\boldsymbol{\sigma}_\mathrm{m}\mathbf{F}_\mathrm{m}^{-c}$), has the form

$$\nabla_{0\mathrm{m}} \cdot \mathbf{P}_\mathrm{m}^{c} = \vec{0}. \tag{3.1}$$

The material behaviour of each microstructural constituent α (e.g. matrix, inclusion etc.) is described by its constitutive law, specifying a time and history dependent stress-strain relationship

$$\mathbf{P}_\mathrm{m}^{(\alpha)}(t) = \boldsymbol{\mathcal{F}}^{(\alpha)}\{\mathbf{F}_\mathrm{m}^{(\alpha)}(\tau), \tau \in [0,t]\}. \tag{3.2}$$

It is emphasized that the present framework is not specifically designed for any particular constitutive law; the microstructural material behaviour may be very complex and include a

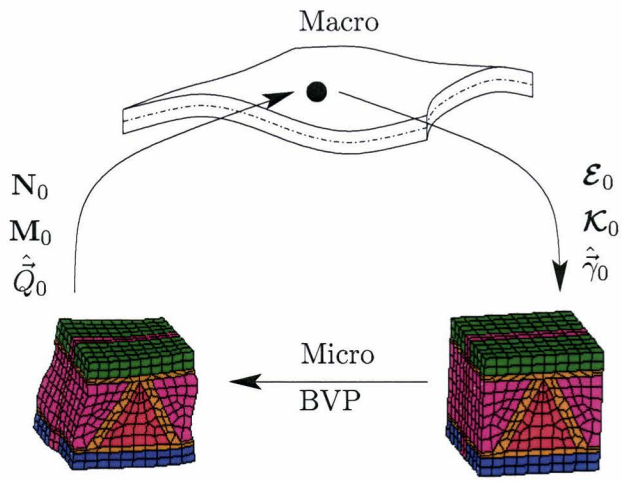

Figure 3.1: Schematic representation of the computational homogenization for structured thin sheets.

physical and/or geometrical evolution of the microstructure (e.g. phase decomposition, phase transformations, decohesion, delamination, inter or intragranular fracture etc.).

The actual position vector $\vec{x}$ of a point in the microstructural RVE is based on (2.7) and (2.9). To account for the effect of a local microscopic displacement field due to microstructural heterogeneities, an unknown microfluctuation field $\vec{w}$ is superimposed on the macroscopic displacement field. For given macroscopic generalized strains, the only unknown contribution to the microstructural displacement field comes from the microfluctuation field $\vec{w}$. Adding boundary conditions for the microfluctuation field completes the microstructural boundary value problem. The kinematical boundary conditions for the Kirchhoff-Love and the Mindlin-Reissner shell-types are described in Sections 3.2.1 and 3.3.1, respectively.

The solution of this boundary value problem may be obtained directly in terms of the unknown microfluctuation field. However, if one wishes to use a general purpose numerical code for the solution of boundary value problems, it is more convenient to reformulate the boundary conditions in terms of the total microstructural displacements, without separation of the coarse and fine scale contributions. This is also done in Sections 3.2.1 and 3.3.1.

3.2 Homogenization towards a Kirchhoff-Love shell-type

3.2.1 Micro-Macro kinematics

The top and bottom surfaces of the shell and thus of the microstructural RVE are traction free surfaces. Therefore, in this research, the top T and bottom D surface of the RVE are required to be traction free

$$\vec{p}_{\mathrm{T}} = \vec{p}_{\mathrm{D}} = \vec{0} \tag{3.3}$$

These traction free top and bottom faces of the RVE leave the strain in the thickness direction undetermined. This condition is typically relevant for shells that are not loaded in the out-of-plane direction, which is the case for e.g. flexible displays or solar cells. The elaboration

of the kinematical boundary conditions for the transverse boundaries of the microstructural RVE are based on the expression for the infinitely small material line element in the current configuration given by the relation (2.7). Where for a KL-shell the transverse shear $\hat{\vec{\gamma}}_0$ is assumed to be zero and the microfluctuation field $\vec{w}$ is superimposed. The in-plane position vector $\Delta\vec{X}$ of a finite yet small material vector line element in the current configuration is written as

$$\Delta\hat{\vec{x}} \;=\; (\hat{\mathbf{I}} + \boldsymbol{\varepsilon}_0 + \zeta\boldsymbol{\kappa}_0)\cdot\Delta\hat{\vec{X}} + \Delta\hat{\vec{w}} \tag{3.4}$$

This relation is applied to an undeformed volume of the microstructural representative cell with respect to its geometrical center $\vec{X}_c$, located in $\vec{x}_c$ after deformation. From a physical point of view the center of the RVE is identified as the macroscopic point on the midsurface, at which the generalized strain tensors are calculated. The RVE volume represents the underlying microstructure in the full thickness of the shell and a finite, yet small, in-plane vicinity of this point. For simplicity the origin of the used Cartesian vector basis is placed at the geometric center of the undeformed RVE, i.e. $\vec{X}_c = \vec{0}$, thus $\Delta\vec{X} = \vec{X} - \vec{X}_c = \vec{X}$ and $\Delta\vec{x} = \vec{x} - \vec{x}_c$.

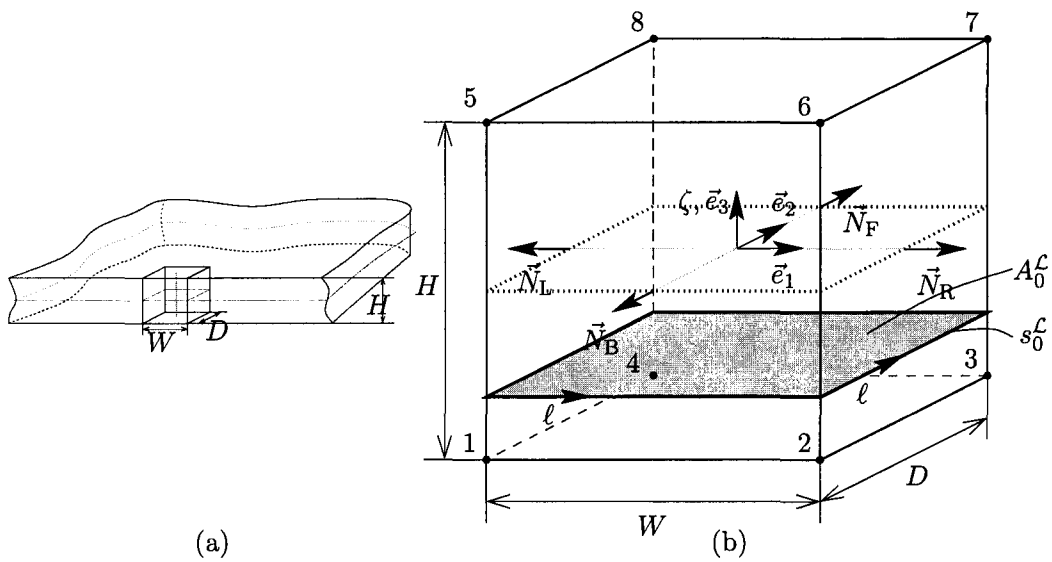

Figure 3.2: (a) The RVE depicted in a shell (b) and the through-thickness representative volume element (RVE).

The kinematical constrains, which are defined in this section apply to the boundaries of a three-dimensional initially rectangular RVE, with width W, depth D, and height H, see Figure 3.2.b. The initial volume of the RVE is denoted by V_0. The initially rectangular RVE represents a periodic in-plane cell of the initially flat macroscopic shell, see Figure 3.2.a. Since the RVE represents the full thickness of the macroscopic structure, H equals the local thickness of the shell. In the undeformed reference state the opposing transverse boundary normals are $\vec{N}_L = -\vec{N}_R$, and $\vec{N}_B = -\vec{N}_F$, where the subscripts L, R, B, and F denote quantities corresponding to the left, right, back, and front boundary of the RVE, respectively. These boundaries are called the transverse boundaries and their combined undeformed area is denoted by $\hat{\Gamma}_0$. The initial area of each lamina $A_0^{\mathcal{L}}(\zeta) = WD$ is equal for each lamina for

this particular choice of RVE, and is schematically depicted in Figure 3.2.b by the gray plane. The intersection line of the transverse boundaries and a lamina is a closed line and is denoted by $s_0^{\mathcal{L}}(\zeta)$.

The in-plane gradient of the in-plane position vector (3.4) of the finite material vector is determined as

$$(\hat{\nabla}_0 \Delta\hat{\vec{x}})^c = \hat{\hat{\mathbf{I}}} + \boldsymbol{\varepsilon}_0 + \zeta\boldsymbol{\kappa}_0 + (\hat{\nabla}_0 \Delta\hat{\vec{w}})^c. \tag{3.5}$$

This deformation gradient tensor $(\hat{\nabla}_0 \Delta\hat{\vec{x}})^c$ represents the in-plane deformation of a lamina at position ζ. In the scale transition in both the classical homogenization theories (e.g. [6, 11]) and the second-order computational homogenization [7], the macroscopic deformation gradient tensor is required to be equal to the RVE volume average of the microstructural deformation gradient tensor. In the homogenization of thin sheets only an in-plane homogenization is required since the homogenization in the through-thickness direction is, in fact, accomplished by the stress resultants definition used in shell theories. Therefore, a modified scale transition relation is proposed that requires the local macroscopic laminair deformation gradient tensor $\hat{\hat{\mathbf{F}}}_{\mathcal{L}}$ to be equal to the surface average (over the undeformed area $A_0^{\mathcal{L}}$ of the lamina) of the microstructural in-plane deformation gradient tensor $(\hat{\nabla}_0 \Delta\hat{\vec{x}})^c$ for each lamina. Hence it is required that,

$$\boldsymbol{\varepsilon}_0 + \zeta\boldsymbol{\kappa}_0 + \hat{\hat{\mathbf{I}}} = \frac{1}{A_0^{\mathcal{L}}} \int_{A_0^{\mathcal{L}}} (\hat{\nabla}_0 \Delta\hat{\vec{x}}(\zeta))^c \mathrm{d}A_0^{\mathcal{L}} \qquad \forall\zeta \in [-H/2, H/2] \tag{3.6}$$

Integrating (3.5) over the area of a lamina and using the divergence theorem to transform the area integral to the integral along the boundary of the lamina, it follows that the condition (3.6) can be satisfied by applying the following constraints on the microfluctuation field $\Delta\hat{\vec{w}}$

$$\int_{s_0^{\mathcal{L}}} \Delta\hat{\vec{w}}(\zeta) \hat{\vec{N}} \mathrm{d}s_0^{\mathcal{L}} = \hat{\vec{0}} \qquad \forall\zeta \in [-H/2, H/2]. \tag{3.7}$$

For an initially periodic RVE, each lamina is also periodic and thus the constraint (3.7) can, for example, be satisfied by requiring the periodicity of the microfluctuation field on the transverse boundaries

$$\Delta\hat{\vec{w}}_{\mathrm{L}}(\ell, \zeta) = \Delta\hat{\vec{w}}_{\mathrm{R}}(\ell, \zeta) \quad \text{and} \quad \Delta\hat{\vec{w}}_{\mathrm{B}}(\ell, \zeta) = \Delta\hat{\vec{w}}_{\mathrm{F}}(\ell, \zeta) \qquad \forall\zeta \in [-H/2, H/2] \tag{3.8}$$

where ℓ is a local coordinate along the edge. Note, however, that the resulting deformation of the RVE, in general, will not be periodic due to the macroscopic higher-order deformation modes (e.g. bending). It can be shown that the in-plane tractions resulting from these constraints are anti-periodic, e.g. $\hat{\vec{p}}_{\mathrm{R}} = -\hat{\vec{p}}_{\mathrm{L}}$.

Since there are no constrains in the $\vec{e}_3$-direction, rigid rotations of the RVE around the $\vec{e}_1$- and $\vec{e}_2$-axis are not explicitly constrained. For example, a compression of the shell along the first direction is imposed on the RVE by the constraints (3.8) by decreasing the in-plane distance between the left and the right boundary. This constrain can also be satisfied by a rigid rotation of the RVE around the $\vec{e}_2$-axis. In other words, if $\hat{\vec{\gamma}}_0^r = \hat{\vec{0}}$ is not used to prescribe boundary conditions on the RVE, the shell is not enforces to remain tangent to the $(\vec{e}_1, \vec{e}_2)$-plane. Because, it is undesirable to introduce traction in the transverse direction, to stay consistent with the assumptions of the Kirchhoff-Love shell theory, only in-plane constraints

are used. The two additional constraints selected to prescribe the average in-plane position of the transverse boundaries are

$$\int_{\Gamma_{0\mathrm{L}}} \Delta w^1_{\mathrm{L}} \mathrm{d}\Gamma_0 = 0 \quad \text{and} \quad \int_{\Gamma_{0\mathrm{B}}} \Delta w^2_{\mathrm{B}} \mathrm{d}\Gamma_0 = 0 \tag{3.9}$$

The resulting traction related to these constraints is constant and has only a component in the $\vec{e}_1$- and $\vec{e}_2$-direction on the left and back boundary, respectively. Because, the tractions resulting from the constraints (3.8) are anti-periodic, it directly follows from the balance of forces on the RVE, that the traction from (3.9) are equal to zero.

The periodicity constraints (3.8) and zero averaged fluctuations along the left and back faces of the RVE (3.9) are now rewritten in terms of the total microstructural displacements. First, relations equivalent to the periodicity conditions are derived. Applying (3.4) to the left and right (and similarly to the back and front) boundaries of the RVE and subtracting the results, with account for the periodicity conditions (3.8), eliminates the unknown $\hat{\vec{x}}_c$ and $\Delta\hat{\vec{w}}$ leads to kinematic constraints between opposite boundaries according to

$$\hat{\vec{x}}_{\mathrm{R}} = \hat{\vec{x}}_{\mathrm{L}} + (\hat{\hat{\mathbf{I}}} + \boldsymbol{\mathcal{E}}_0 + \zeta\boldsymbol{\mathcal{K}}_0) \cdot W\vec{N}_{\mathrm{R}}, \qquad \hat{\vec{x}}_{\mathrm{F}} = \hat{\vec{x}}_{\mathrm{B}} + (\hat{\hat{\mathbf{I}}} + \boldsymbol{\mathcal{E}}_0 + \zeta\boldsymbol{\mathcal{K}}_0) \cdot D\vec{N}_{\mathrm{F}} \tag{3.10}$$

Next, applying (3.4) to position vectors on the left and back faces at the RVE and integrating the results over the area of the respective face, allows to rewrite the constraints (3.9), prescribing zero averaged fluctuations along the left and back boundary, as

$$\begin{aligned}
\int_{\Gamma_{0\mathrm{L}}} \Delta x^1_{\mathrm{L}} \mathrm{d}\Gamma_0 &= \left\{ (\hat{\hat{\mathbf{I}}} + \boldsymbol{\mathcal{E}}_0) \cdot \int_{\Gamma_{0\mathrm{L}}} \hat{\vec{X}}_{\mathrm{L}} \mathrm{d}\Gamma_0 + \boldsymbol{\mathcal{K}}_0 \cdot \int_{\Gamma_{0\mathrm{L}}} \zeta \hat{\vec{X}}_{\mathrm{L}} \mathrm{d}\Gamma_0 \right\} \cdot \vec{e}_1 \\
\int_{\Gamma_{0\mathrm{B}}} \Delta x^2_{\mathrm{B}} \mathrm{d}\Gamma_0 &= \left\{ (\hat{\hat{\mathbf{I}}} + \boldsymbol{\mathcal{E}}_0) \cdot \int_{\Gamma_{0\mathrm{B}}} \hat{\vec{X}}_{\mathrm{B}} \mathrm{d}\Gamma_0 + \boldsymbol{\mathcal{K}}_0 \cdot \int_{\Gamma_{0\mathrm{B}}} \zeta \hat{\vec{X}}_{\mathrm{B}} \mathrm{d}\Gamma_0 \right\} \cdot \vec{e}_2
\end{aligned} \tag{3.11}$$

3.2.2 Stress and couple-stress resultants

The obtained micro-scale stress state is homogenized towards a 3D macroscopic shell structure based on the Hill-Mandel macrohomogeneity condition [11]. In general, this condition requires the microscopic volume average of the variation of work performed on an RVE to be equal the local variation of the work on the macroscale. In shell theories all macroscopic stress quantities are resultants obtained by a through-thickness integration. Therefore, the Hill-Mandel condition is modified and now requires the variation of the overall microscopic work $\delta W_{0\mathrm{m}}$ performed on an RVE per unit area of midsurface to be equal to the variation of work $\delta W_{0\mathrm{M}}$ on the macroscale per unit of area midsurface.

Equation (2.26) defined the virtual work δW_{M} per unit area of midsurface in the current configuration. The virtual work per unit area of midplane in the reference configuration for the KL shell is given by

$$\delta W_{0\mathrm{M}} = \hat{J}\delta W_{\mathrm{M}} = \mathbf{N}_0 : \delta\boldsymbol{\mathcal{E}}^c_0 + \mathbf{M}_0 : \delta\boldsymbol{\mathcal{K}}^c_0 \tag{3.12}$$

The cubic RVE depicted in Figure 3.2b represents an in-plane area of $A_0 = WD$, therefore, the averaged microscopic virtual work per unit midsurface can be written as

$$\delta W_{0\mathrm{m}} = \frac{1}{A_0} \int_{V_0} \mathbf{P}_{\mathrm{m}} : (\nabla_{0\mathrm{m}} \delta\Delta\vec{x}) \mathrm{d}V_0 \tag{3.13}$$

Thus, the modified Hill-Mandel condition for a shell-type continuum reads

$$\mathbf{N}_0 : \delta\boldsymbol{\mathcal{E}}_0^c + \mathbf{M}_0 : \delta\boldsymbol{\mathcal{K}}_0^c = \frac{1}{A_0}\int_{V_0} \mathbf{P}_\mathrm{m} : (\nabla_{0\mathrm{m}}\delta\Delta\vec{x})\mathrm{d}V_0, \qquad \forall\delta\Delta\vec{x} \tag{3.14}$$

This Hill-Mandel condition can be used to obtain the averaging micro-macro relations for the stress and couple stress resultants.

Using the divergence theorem, with incorporation of equilibrium in the microstructure (3.1), the microstructural work $\delta W_{0\mathrm{m}}$ (per unit of area of the reference plane in the undeformed state A_0) can be written as

$$\delta W_{0\mathrm{m}} = \frac{1}{A_0}\int_{V_0} \mathbf{P}_\mathrm{m} : (\nabla_{0\mathrm{m}}\delta\Delta\vec{x})\mathrm{d}V_0 = \frac{1}{A_0}\int_{\Gamma_0} \vec{p}\cdot\delta\Delta\vec{x}\mathrm{d}\Gamma_0 \tag{3.15}$$

where $\vec{p} = \vec{N}\cdot\mathbf{P}_\mathrm{m}^c$ represents the first Piola-Kirchhoff stress vector and Γ_0 is the whole undeformed surface of the RVE. The out-of-plane component $\tilde{p}$ of the traction on the transverse boundaries is zero. (There are no constrains on these boundaries in the out-of-plane direction). Also, the top and bottom faces of the shell, and consequently of the RVE, are traction free. Taking into account that these (partially) traction free RVE faces do not contribute to the averaged microscopic variation of work and substituting the variation of relation (3.4) leads to

$$\delta W_{0M} = \frac{1}{A_0}\int_{\hat{\Gamma}_0} \hat{\vec{p}}\hat{\vec{X}}\mathrm{d}\hat{\Gamma}_0 : \delta\boldsymbol{\mathcal{E}}_0^c + \frac{1}{A_0}\int_{\hat{\Gamma}_0} \zeta\hat{\vec{p}}\hat{\vec{X}}\mathrm{d}\hat{\Gamma}_0 : \delta\boldsymbol{\mathcal{K}}_0^c + \frac{1}{A_0}\int_{\hat{\Gamma}_0} \hat{\vec{p}}\cdot\delta\Delta\hat{\vec{w}}\mathrm{d}\hat{\Gamma}_0 \tag{3.16}$$

where $\hat{\Gamma}_0$ is the combined area of the transverse boundaries in the undeformed configuration. It is straightforward to show that there is no contribution of the microfluctuation field to the averaged microscopic work, so the last term in (3.16) vanishes. After substitution of (3.16) into the Hill-Mandel condition (3.14) the micro-macro transition relation for the stress and couple-stress resultants follow as

$$\mathbf{N}_0 = \frac{1}{A_0}\int_{\hat{\Gamma}_0} \hat{\vec{p}}\hat{\vec{X}}\mathrm{d}\hat{\Gamma}_0 \tag{3.17}$$

$$\mathbf{M}_0 = \frac{1}{A_0}\int_{\hat{\Gamma}_0} \zeta\hat{\vec{p}}\hat{\vec{X}}\mathrm{d}\hat{\Gamma}_0 \tag{3.18}$$

The boundary integrals allow the computation of the macroscopic stress resultants based on microstructural variables defined on the RVE transverse boundaries only. Taking into account that the out-of-plane components of the microscopic first Piola-Kirchhoff stress tensor are zero, the relations (3.17) and (3.18) can also be transformed into volume integrals

$$\mathbf{N}_0 = \frac{1}{A_0}\int_{V_0} \hat{\mathbf{P}}_\mathrm{m}\mathrm{d}V_0 = \int_H \left(\frac{1}{A_0^{\mathcal{L}}}\int_{A_0^{\mathcal{L}}} \hat{\mathbf{P}}_\mathrm{m}\mathrm{d}A_0^{\mathcal{L}}\right)\mathrm{d}H \tag{3.19}$$

$$\mathbf{M}_0 = \frac{1}{A_0}\int_{V_0} \zeta\hat{\mathbf{P}}_\mathrm{m}\mathrm{d}V_0 = \int_H \left(\frac{1}{A_0^{\mathcal{L}}}\int_{A_0^{\mathcal{L}}} \zeta\hat{\mathbf{P}}_\mathrm{m}\mathrm{d}A_0^{\mathcal{L}}\right)\mathrm{d}H \tag{3.20}$$

where for clarity the volume integrals are divided into an averaging integrale over each lamina and an integration over the initial height of the RVE. Comparing definitions (2.27) and (2.28) of the classical resultant tensor to the volume integrals in (3.19) and (3.20), it shows that in addition to the through thickness integration, there is an in-plane averaging. The calculated in-plane surface averages are, in fact, the desired in-plane homogenization.

3.3 Homogenization towards a Mindlin-Reissner shell-type

3.3.1 Micro-Macro kinematics

The top and bottom surfaces of a Mindlin-Reissner type RVE are also required to be traction free (3.3). The derivation of the kinematical boundary conditions for the microstructural RVE for the macroscopic shell of MR-type again starts from the in-plane position vector (2.7) with addition of a microfluctuation field

$$\Delta\hat{\vec{x}} = (\hat{\hat{\mathbf{I}}} + \boldsymbol{\mathcal{E}}_0 + \zeta\boldsymbol{\mathcal{K}}_0) \cdot \Delta\hat{\vec{X}} + \zeta\hat{\vec{\gamma}}_0 + \Delta\hat{\vec{w}} \tag{3.21}$$

The requirement (3.6) that the average of the in-plane laminair strain equals the laminair strain defined by the macroscopic deformation tensors $\boldsymbol{\mathcal{E}}_0$ and $\boldsymbol{\mathcal{K}}_0$ again leads to the periodicity conditions on the in-plane microfluctuation field (3.8) for the initially rectangular RVE, as described in Section 3.2.1.

In addition to the laminair strain, transverse shears $\hat{\vec{\gamma}}_0$ should be prescribed for a MR-type shell. The shell theories on one hand assume the fibers to remain straight but on the other hand, the absence of a global shear traction in the micro-scale problem inhibit the directors from remaining straight, see Figure 3.3.

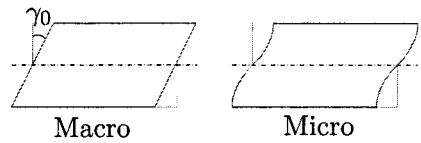

Figure 3.3: Macro-micro inconsistency for transverse shear

Therefore, in the macro-micro scale transition the fibers are no longer assumed to be rigid. The philosophy for the scale transition of the transverse shear is the requirement that the average "displacement moment" of a fiber is preserved. The displacement moment is defined as the product of the in-plane displacement $\hat{\vec{u}}$ and the initial distance of a point to midsurface, ζ. Hence

$$\int_H \zeta\hat{\vec{u}}\mathrm{d}H = \int_H \zeta(\zeta\hat{\vec{\gamma}}_0)\mathrm{d}H \tag{3.22}$$

Substitution of (3.21) in (3.22) and evaluating the integral along the considered fiber ($\hat{\vec{X}} = \hat{\vec{0}}$) and by taking into account that $\boldsymbol{\mathcal{E}}_0$, $\boldsymbol{\mathcal{K}}_0$ and $\hat{\vec{\gamma}}_0$ are constant for each point along the fiber gives

$$\int_H \zeta\Delta\hat{\vec{w}}\mathrm{d}H = \hat{\vec{0}} \tag{3.23}$$

In other words, the "displacement moment" produced by the microfluctuationfield along a fier should be zero for the postulated scale transition. Since the RVE represents a finite vicinity of a fiber, and since we want to formulate all macro-micro relations in terms of boundary relations, this relation will be prescribed to each of the transverse boundaries of the RVE separately, but according to the periodicity conditions only two are needed.

$$\int_{\Gamma_{0\mathrm{L}}} \zeta\Delta\hat{\vec{w}}_{\mathrm{L}}\mathrm{d}\Gamma_0 = \hat{\vec{0}} \quad \text{and} \quad \int_{\Gamma_{0\mathrm{B}}} \zeta\Delta\hat{\vec{w}}_{\mathrm{B}}\mathrm{d}\Gamma_0 = \hat{\vec{0}} \tag{3.24}$$

The constraints of equation (3.24) introduces the difference in moment on two opposing boundaries necessary for transverse shear. When the in-plane dimensions of the RVE are small compared with its thickness ($W, D < H$), the resulting deformation of the RVE approaches the deformation of a single fiber described above. For larger in-plane dimensions the RVE is more flexible in bending compared to transverse shear (see Section 5.1.1). The dependence of the transverse shear stiffness on the RVE size originates from applying relations valid for a fiber on an RVE of the finite vicinity around the fiber.

The moment on the RVE that results from (3.24) should be counterbalanced by transverse shear traction on the transverse boundaries. Based on (2.9), the transverse position vector of finite material vector $\Delta\vec{X}$ in the current configuration is

$$\Delta\tilde{\vec{u}} = \vec{e}_3\hat{\vec{\gamma}}_0^r \cdot \Delta\hat{\vec{X}} - \tfrac{1}{2}\vec{e}_3\boldsymbol{\mathcal{K}}_0 : \Delta\hat{\vec{X}}\Delta\hat{\vec{X}} + \Delta\tilde{\vec{w}} \tag{3.25}$$

Note, that $\hat{\vec{\gamma}}_0^r$ is not a generalized strain, it represents the in-plane gradient of the transverse displacements. Since, the lamina are assumed to remain tangent to the ($\vec{e}_1$,$\vec{e}_2$)-plane, $\hat{\vec{\gamma}}_0^r$ is an in-plane zero vector $\hat{\vec{0}}$. Again, the modified scale transition relation is used that requires the local macroscopic in-plane deformation gradient tensor to be equal to the surface average of the microstructural in-plane deformation gradient tensor $(\hat{\nabla}_0\Delta\tilde{\vec{x}})^c$ for each lamina. Here, the surface average of the in-plane gradient of the transverse deformation is considered. The macroscopic gradient transverse-deformation tensor is $\hat{\vec{\gamma}}_0^r\vec{e}_3$, when taken into account that $\int_{V_0}\hat{\vec{X}}\mathrm{d}V_0 = \hat{\vec{0}}$. The scale transition relation now reads

$$\frac{1}{A_0^{\mathcal{L}}}\int_{A_0^{\mathcal{L}}}(\hat{\nabla}_0\Delta\tilde{\vec{u}}(\zeta))^c\mathrm{d}A_0^{\mathcal{L}} = \hat{\vec{\gamma}}_0\vec{e}_3 + \frac{1}{A_0^{\mathcal{L}}}\int_{A_0^{\mathcal{L}}}(\hat{\nabla}_0\Delta\tilde{\vec{w}}(\zeta))^c\mathrm{d}A_0^{\mathcal{L}} \qquad \forall\zeta\in[-H/2, H/2] \tag{3.26}$$

This macro-micro scale transition requires that the contribution of the microfluctuation field to this surface average is zero. Again, the choice is made to satisfy this relation by constraining the transverse microfluctuation field by the periodicity conditions

$$\Delta\tilde{\vec{w}}_{\mathrm{L}}(\ell,\zeta) = \Delta\tilde{\vec{w}}_{\mathrm{R}}(\ell,\zeta) \quad \text{and} \quad \Delta\tilde{\vec{w}}_{\mathrm{B}}(\ell,\zeta) = \Delta\tilde{\vec{w}}_{\mathrm{F}}(\ell,\zeta) \tag{3.27}$$

Constraint (3.27) causes the tangent of each lamina to remain parallel to the $(\vec{e}_1, \vec{e}_2)$-plane, whereas the overall thickness change of the RVE is not confined.

Finally, the kinematical boundary condition derived for the MR-shell are also written in terms of total microstructural position vector. The periodicity conditions (3.10) derived for the KL shell-type also apply for the MR shell-type. The boundary integrals prescribing zero averaged "fluctuation moment" (3.24) along the left and back boundary are rewritten as

$$\begin{aligned}
\int_{\Gamma_{0\mathrm{L}}}\zeta\Delta\hat{\vec{x}}_{\mathrm{L}}\mathrm{d}\Gamma_0 &= (\hat{\hat{\mathbf{I}}}+\boldsymbol{\mathcal{E}}_0)\cdot\int_{\Gamma_{0\mathrm{L}}}\zeta\hat{\vec{X}}_{\mathrm{L}}\mathrm{d}\Gamma_0 + \boldsymbol{\mathcal{K}}_0\cdot\int_{\Gamma_{0\mathrm{L}}}\zeta^2\hat{\vec{X}}_{\mathrm{L}}\mathrm{d}\Gamma_0 + \hat{\vec{\gamma}}_0\int_{\Gamma_{0\mathrm{L}}}\zeta^2\mathrm{d}\Gamma_0 \\
\int_{\Gamma_{0\mathrm{B}}}\zeta\Delta\hat{\vec{x}}_{\mathrm{B}}\mathrm{d}\Gamma_0 &= (\hat{\hat{\mathbf{I}}}+\boldsymbol{\mathcal{E}}_0)\cdot\int_{\Gamma_{0\mathrm{B}}}\zeta\hat{\vec{X}}_{\mathrm{B}}\mathrm{d}\Gamma_0 + \boldsymbol{\mathcal{K}}_0\cdot\int_{\Gamma_{0\mathrm{B}}}\zeta^2\hat{\vec{X}}_{\mathrm{B}}\mathrm{d}\Gamma_0 + \hat{\vec{\gamma}}_0\int_{\Gamma_{0\mathrm{B}}}\zeta^2\mathrm{d}\Gamma_0
\end{aligned} \tag{3.28}$$

Finally, applying (3.25) to the left and right (and similarly to the back and front) boundaries of the RVE an subtracting the results, with account for the periodicity conditions (3.27), eliminates the unknown $\tilde{\vec{x}}_c$ and $\Delta\tilde{\vec{w}}$ leads to kinematic constraints between opposing boundaries according to

$$\begin{aligned}
\tilde{\vec{u}}_{\mathrm{R}} &= \tilde{\vec{u}}_{\mathrm{L}} + \vec{e}_3\hat{\vec{\gamma}}_0^r\cdot W\vec{N}_{\mathrm{R}} - \frac{1}{2}\vec{e}_3\boldsymbol{\mathcal{K}}_0 : (\hat{\vec{X}}_{\mathrm{R}}\hat{\vec{X}}_{\mathrm{R}} - \hat{\vec{X}}_{\mathrm{L}}\hat{\vec{X}}_{\mathrm{L}}) \\
\tilde{\vec{u}}_{\mathrm{F}} &= \tilde{\vec{u}}_{\mathrm{B}} + \vec{e}_3\hat{\vec{\gamma}}_0^r\cdot T\vec{N}_{\mathrm{F}} - \frac{1}{2}\vec{e}_3\boldsymbol{\mathcal{K}}_0 : (\hat{\vec{X}}_{\mathrm{F}}\hat{\vec{X}}_{\mathrm{F}} - \hat{\vec{X}}_{\mathrm{B}}\hat{\vec{X}}_{\mathrm{B}}).
\end{aligned} \tag{3.29}$$

3.3.2 Stress and couple-stress resultants

The Hill-Mandel condition will again be used to homogenize the micro-scale stress state towards the desired macroscopic stress resultants. The stress resultants defined in the Hill-Mandel condition of a MR shell-type are the the macroscopic stress $\mathbf{N}_0$, couple-stress $\mathbf{M}_0$ resultant tensors and the shear stress resultant $\hat{\vec{Q}}_0$. Therefore, for the MR-shell the Hill-mandel condition has the form.

$$\frac{1}{A_0}\int_{V_0} \mathbf{P}_{\mathrm{m}} : (\nabla_{0\mathrm{m}}\delta\Delta\vec{x})\mathrm{d}V_0 = \mathbf{N}_0 : \delta\boldsymbol{\mathcal{E}}_0^c + \mathbf{M}_0 : \delta\boldsymbol{\mathcal{K}}_0^c + \hat{\vec{Q}}_0^1 \cdot \delta\hat{\vec{\gamma}}_0 + \hat{\vec{Q}}_0^2 \cdot \delta\hat{\vec{\gamma}}_0^r \tag{3.30}$$

The divergence theorem is again used to rewrite the left-hand side of equation (3.30) as a boundary integral (3.15) to represent the microstructural work $\delta W_{0\mathrm{m}}$ per unit area of midplane. The top and bottom surfaces are traction free, and therefore do not contribute to the virtual work. The variables defined in the transverse boundary integrals are divided into in-plane and transverse components and the displacement relations of equations (3.21) and (3.25) are substituted.

$$\begin{aligned}\delta W_{0\mathrm{m}} &= \frac{1}{A_0}\int_{\hat{\Gamma}_0} \hat{\vec{p}} \cdot \left\{(\delta\boldsymbol{\mathcal{E}}_0 + \zeta\delta\boldsymbol{\mathcal{K}}_0)\cdot\hat{\vec{X}}_r + \zeta\delta\hat{\vec{\gamma}}_0 + \delta\Delta\hat{\vec{w}}\right\}\mathrm{d}\hat{\Gamma}_0 \\ &\quad + \frac{1}{A_0}\int_{\hat{\Gamma}_0} \tilde{\vec{p}} \cdot \left\{\vec{e}_3\delta\hat{\vec{\gamma}}_0^r \cdot \hat{\vec{X}} - \frac{1}{2}\vec{e}_3\delta\boldsymbol{\mathcal{K}}_0 : \hat{\vec{X}}\hat{\vec{X}} + \delta\Delta\tilde{\vec{w}}\right\}\mathrm{d}\hat{\Gamma}_0\end{aligned} \tag{3.31}$$

The virtual work performed by the microfluactuation field again can be shown to be zero, and thus may be canceled out of equation (3.31). Comparing (3.31) and the right-hand side of (3.30), the relations for the macroscopic stress resultant $\mathbf{N}_0$ and the resultant couple stress $\mathbf{M}_0$ tensors are obtained as

$$\mathbf{N}_0 = \frac{1}{A_0}\int_{\hat{\Gamma}_0} \hat{\vec{p}}\hat{\vec{X}}\mathrm{d}\hat{\Gamma}_0 \tag{3.32}$$

$$\mathbf{M}_0 = \frac{1}{A_0}\int_{\hat{\Gamma}_0} (\zeta\hat{\vec{p}}\hat{\vec{X}} - \tfrac{1}{2}\tilde{\vec{p}}\cdot\vec{e}_3\hat{\vec{X}}\hat{\vec{X}})\mathrm{d}\hat{\Gamma}_0 \tag{3.33}$$

The recovered definition of the macroscopic stress resultant is the same for the KL and the MR shell-type. The definition of the macroscopic couple-stress resultant of the MR shell-type obtained an extra term compared to the KL-definition. This term arises from the traction in the transverse direction, which also may contribute to the bending moment. The obtained shear resultants $\hat{\vec{Q}}_0^1$ and $\hat{\vec{Q}}_0^2$ are

$$\hat{\vec{Q}}_0^1 = \frac{1}{A_0}\int_{\hat{\Gamma}_0} \zeta\hat{\vec{p}}\mathrm{d}\hat{\Gamma}_0 \tag{3.34}$$

$$\hat{\vec{Q}}_0^2 = \frac{1}{A_0}\int_{\hat{\Gamma}_0} \tilde{\vec{p}}\cdot\vec{e}_3\hat{\vec{X}}\mathrm{d}\hat{\Gamma}_0 \tag{3.35}$$

The transverse shear stress resultant of equation (3.34) represents the in-plane gradient of moment applied to the RVE. The transverse shear stress resultant of equation (3.35) represents the transverse shear necessary to counterbalance this gradient. The macroscopic transverse shear component is defined as

$$\hat{\vec{Q}}_0 = \tfrac{1}{2}(\hat{\vec{Q}}_0^1 + \hat{\vec{Q}}_0^2) \tag{3.36}$$

Chapter 4

Numerical implementation

In this research the microstructural boundary value problem outlined in the previous chapter is solved by the finite element method. The boundary conditions of the microstructural RVE are elaborated in more detail in Section 4.1. The method used to prescribe the boundary conditions provides an efficient way to calculate the generalized stress resultants and the macroscopic stiffness matrices. This will be described in Section 4.2.

4.1 Solution of the microscale problem

The microstructural boundary value problem outlined in Section 3.1 is a standard non-linear quasi-static boundary value problem for a classical three-dimensionall continuum. As it was the case in the previous section, here the attention remains focused on the three-dimensional rectangular RVE, schematically depicted in Figure 3.2b. Using a standard finite element procedure, the weak form of the equilibrium for the microlevel RVE (after discretization) leads to a system of non-linear algebraic equations in the nodal displacements $\underset{\sim}{u}$

$$\underset{\sim}{f}_{int}(\underset{\sim}{u}) = \underset{\sim}{f}_{ext} \tag{4.1}$$

expressing the balance of internal and external nodal forces. This system has to be complemented by boundary conditions. Hence, the application of the earlier introduced boundary conditions of the Kirchhoff-Love-type RVE, (3.10) and (3.11) and the Mindlin-Reissner-type RVE, (3.10), (3.28), and (3.29), have to be elaborated in more detail.

4.1.1 Boundary value problem for Kirchhoff-Love-type RVE

The kinematics derived in the previous chapter are with respect to the unknown position of the center of the RVE in the deformed state $\vec{x}_c$. This rigid body translation is easily suppressed by spatial fixation of the displacement of one node, say corner node $i = 1$. Taking into account that $\vec{X}_c = \vec{0}$. When is assumed that the $\Delta\vec{w}_1 = \vec{0}$, the in-plane part of the center in the current configuration $\hat{\vec{x}}_c$ can obtained from (3.4)

$$\hat{\vec{x}}_c \;=\; \hat{\vec{X}}_1 - (\hat{\mathbf{I}} + \boldsymbol{\varepsilon}_0 + \zeta_1 \boldsymbol{\kappa}_0) \cdot \hat{\vec{X}}_1 \tag{4.2}$$

By making use of the generalized in-plane periodicity constraint (3.10), the in-plane positions of the corner nodes on the bottom surface of the RVE can be written as (see Figure

3.2b for the numbering of nodes used)

$$\hat{\vec{u}}_i = (\boldsymbol{\mathcal{E}}_0 + \zeta_1 \boldsymbol{\mathcal{K}}_0) \cdot (\hat{\vec{X}}_i - \hat{\vec{X}}_1), \qquad i = 1, 2, 4 \tag{4.3}$$

Similarly the relative displacement of the corner points of the top face of the RVE can be expressed in terms of generalized strains.

$$\begin{aligned} \hat{\vec{u}}_{\widehat{56}} &= \hat{\vec{u}}_6 - \hat{\vec{u}}_5 = (\boldsymbol{\mathcal{E}}_0 + \zeta_5 \boldsymbol{\mathcal{K}}_0) \cdot (\hat{\vec{X}}_6 - \hat{\vec{X}}_5), \\ \hat{\vec{u}}_{\widehat{58}} &= \hat{\vec{u}}_8 - \hat{\vec{u}}_5 = (\boldsymbol{\mathcal{E}}_0 + \zeta_5 \boldsymbol{\mathcal{K}}_0) \cdot (\hat{\vec{X}}_8 - \hat{\vec{X}}_5) \end{aligned} \tag{4.4}$$

The relative in-plane displacement of two opposing points (3.10) only linearly depends on their initial distance to the reference plane ζ. These constraints (3.10) can be recast in terms of in-plane displacements as

$$\begin{aligned} \hat{\vec{u}}_{\mathrm{R}} &= \hat{\vec{u}}_{\mathrm{L}} + \tfrac{1}{2}(1-\eta)(\hat{\vec{u}}_2 - \hat{\vec{u}}_1) + \tfrac{1}{2}(1+\eta)\hat{\vec{u}}_{\widehat{56}}, \\ \hat{\vec{u}}_{\mathrm{F}} &= \hat{\vec{u}}_{\mathrm{B}} + \tfrac{1}{2}(1-\eta)(\hat{\vec{u}}_4 - \hat{\vec{u}}_1) + \tfrac{1}{2}(1+\eta)\hat{\vec{u}}_{\widehat{58}}, \\ \hat{\vec{u}}_{\mathrm{RF}} &= \hat{\vec{u}}_{\mathrm{LB}} + \tfrac{1}{2}(1-\eta)(\hat{\vec{u}}_2 + \hat{\vec{u}}_4 - 2\hat{\vec{u}}_1) + \tfrac{1}{2}(1+\eta)(\hat{\vec{u}}_{\widehat{56}} + \hat{\vec{u}}_{\widehat{58}}) \end{aligned} \tag{4.5}$$

with $\eta = \frac{2\zeta}{H}$ the local coordinate of the corresponding points on the right - left ($\mathrm{R}-\mathrm{L}$), front - back ($\mathrm{F}-\mathrm{B}$) boundaries and on the right,front - left,back ($\mathrm{RF}-\mathrm{LB}$) edges. The in-plane vectors $\hat{\vec{u}}_{(i)}$, $i = 1, 2, 4, \widehat{56}, \widehat{58}$ are prescribed according to (4.3), and (4.4). For an RVE that has an equal distribution of nodes on two opposing transverse boundaries in the undeformed state, relations (4.5) lead to a set of homogeneous constraints (tyings).

Boundary constraints (3.11) prescribing the zero-averaged microstructural fluctuations normal the undeformed boundary, may be rewritten in terms of corresponding displacement components of the nodes on the boundary

$$\sum_{i=1}^{n_{\mathrm{L}}} \alpha^i u_{\mathrm{L}}^{i1} = u_{\mathrm{L}^*}^1(\boldsymbol{\mathcal{E}}_0, \boldsymbol{\mathcal{K}}_0), \qquad \sum_{i=1}^{n_{\mathrm{B}}} \beta^i u_{\mathrm{B}}^{i2} = u_{\mathrm{B}^*}^2(\boldsymbol{\mathcal{E}}_0, \boldsymbol{\mathcal{K}}_0) \tag{4.6}$$

where n_{L} and n_{B} are the numbers of nodes on the left and back boundary, respectively; α^i and β^i are coefficients following from the discretized form of the left-hand sides of (3.11); $u_{\mathrm{L}^*}^1$ and $u_{\mathrm{B}^*}^2$ are scalars form the right-hand side of (3.11). Eliminating $\hat{\vec{x}}_c$ according to (4.2) gives for $u_{\mathrm{L}^*}^1$ and $u_{\mathrm{B}^*}^2$

$$\begin{aligned} u_{\mathrm{L}^*}^1 &= \left\{ \boldsymbol{\mathcal{E}}_0 \cdot \int_{\Gamma_{0\mathrm{L}}} (\hat{\vec{X}}_{\mathrm{L}} - \hat{\vec{X}}_1) \mathrm{d}\Gamma_0 + \boldsymbol{\mathcal{K}}_0 \cdot \int_{\Gamma_{0\mathrm{L}}} (\zeta_{\mathrm{L}} \hat{\vec{X}}_{\mathrm{L}} - \zeta_1 \hat{\vec{X}}_1) \mathrm{d}\Gamma_0 \right\} \cdot \vec{e}_1 \\ u_{\mathrm{B}^*}^2 &= \left\{ \boldsymbol{\mathcal{E}}_0 \cdot \int_{\Gamma_{0\mathrm{B}}} (\hat{\vec{X}}_{\mathrm{B}} - \hat{\vec{X}}_1) \mathrm{d}\Gamma_0 + \boldsymbol{\mathcal{K}}_0 \cdot \int_{\Gamma_{0\mathrm{B}}} (\zeta_{\mathrm{B}} \hat{\vec{X}}_{\mathrm{B}} - \zeta_1 \hat{\vec{X}}_1) \mathrm{d}\Gamma_0 \right\} \cdot \vec{e}_2 \end{aligned} \tag{4.7}$$

Consequently, the scalars $u_{\mathrm{L}^*}^1$ and $u_{\mathrm{B}^*}^2$ are known for any given $\boldsymbol{\mathcal{E}}_0$ and $\boldsymbol{\mathcal{K}}_0$ and the RVE geometry. Contrary to the constraints (4.5), which gave rise to homogeneous tying relation, the constraints (4.6) result in a set of non-homogeneous constraints.

4.1.2 Boundary value problem for Mindlin-Reissner-type RVE

The solution of the microstructural boundary value problem for the Mindlin-Reissner-type RVE is also obtained by discretization of the boundary constraints.The corner node $i = 1$ is again spatially fixated and the in-plane position of the RVE's center $\hat{\vec{x}}_c$ and the transverse position $\tilde{\vec{x}}_c$ are determined according to (3.21) and (3.25), respectively

$$\hat{\vec{x}}_c = \hat{\vec{X}}_1 - (\hat{\vec{\mathbf{I}}} + \boldsymbol{\mathcal{E}}_0 + \zeta_1 \boldsymbol{\mathcal{K}}_0) \cdot \hat{\vec{X}}_1 - \zeta_1 \hat{\vec{\gamma}}_0 \tag{4.8}$$

$$\tilde{\vec{x}}_c = \tilde{\vec{X}}_1 - \vec{e}_3 \hat{\vec{\gamma}}_0^T \cdot \hat{\vec{X}}_1 + \tfrac{1}{2} \vec{e}_3 \boldsymbol{\mathcal{K}}_0 : \hat{\vec{X}}_1 \hat{\vec{X}}_1 \tag{4.9}$$

The generalized periodic in-plane constraint (3.10), again can be rewritten to a homogeneous linear set of equations (4.5) related to the in-plane positions of the corner nodes on the bottom surface of the RVE

$$\hat{\vec{u}}_i = (\boldsymbol{\mathcal{E}}_0 + \zeta_1 \boldsymbol{\mathcal{K}}_0) \cdot (\hat{\vec{X}}_i - \hat{\vec{X}}_1) + (\zeta_i - \zeta_1) \hat{\vec{\gamma}}_0, \qquad i = 1, 2, 4 \tag{4.10}$$

The boundary integrals prescribing zero averaged "fluctuation moment" (3.28) , that enforce the in-plane transverse shear are rewritten in terms of displacement vectors of the nodes on the left L and back B boundaries

$$\sum_{i=1}^{n_{\mathrm{L}}} \alpha^i \zeta^i \hat{\vec{u}}_{\mathrm{L}}^i = \hat{\vec{u}}_{\mathrm{L}^{**}}(\boldsymbol{\mathcal{E}}_0, \boldsymbol{\mathcal{K}}_0, \hat{\vec{\gamma}}_0), \qquad \sum_{i=1}^{n_{\mathrm{B}}} \beta^i \zeta^i \hat{\vec{u}}_{\mathrm{B}}^i = \hat{\vec{u}}_{\mathrm{B}^{**}}(\boldsymbol{\mathcal{E}}_0, \boldsymbol{\mathcal{K}}_0, \hat{\vec{\gamma}}_0) \tag{4.11}$$

where $\hat{\vec{u}}_{\mathrm{L}^{**}}$ and $\hat{\vec{u}}_{\mathrm{B}^{**}}$ are in-plane vectors from the right-hand sides of (3.28). The in-plane position of the center of the RVE $\hat{\vec{x}}_c$ is eliminated by making use of (4.8)

$$\begin{aligned}
\hat{\vec{u}}_{\mathrm{L}^{**}} &= \boldsymbol{\mathcal{E}}_0 \cdot \int_{\Gamma_{0\mathrm{L}}} \zeta_{\mathrm{L}} (\hat{\vec{X}}_{\mathrm{L}} - \hat{\vec{X}}_1) \mathrm{d}\Gamma_0 + \boldsymbol{\mathcal{K}}_0 \cdot \int_{\Gamma_{0\mathrm{L}}} (\zeta_{\mathrm{L}} \hat{\vec{X}}_{\mathrm{L}} - \zeta_1 \hat{\vec{X}}_1) \mathrm{d}\Gamma_0 + \hat{\vec{\gamma}}_0 \int_{\Gamma_{0\mathrm{L}}} \zeta_{\mathrm{L}} (\zeta_{\mathrm{L}} - \zeta_1) \mathrm{d}\Gamma_0 \\
\hat{\vec{u}}_{\mathrm{B}^{**}} &= \boldsymbol{\mathcal{E}}_0 \cdot \int_{\Gamma_{0\mathrm{B}}} \zeta_{\mathrm{B}} (\hat{\vec{X}}_{\mathrm{B}} - \hat{\vec{X}}_1) \mathrm{d}\Gamma_0 + \boldsymbol{\mathcal{K}}_0 \cdot \int_{\Gamma_{0\mathrm{B}}} (\zeta_{\mathrm{B}} \hat{\vec{X}}_{\mathrm{B}} - \zeta_1 \hat{\vec{X}}_1) \mathrm{d}\Gamma_0 + \hat{\vec{\gamma}}_0 \int_{\Gamma_{0\mathrm{B}}} \zeta_{\mathrm{B}} (\zeta_{\mathrm{B}} - \zeta_1) \mathrm{d}\Gamma_0
\end{aligned} \tag{4.12}$$

In addition to the in-plane generalized periodic displacement also transverse generalized periodic displacements (3.29) are imposed on the MR-RVE. By making use of the transverse fixation of the displacement of node 1 and the transverse periodicity constraints, the displacement of the corner nodes $j = 1, 2, 3, 4$ can be written as

$$\tilde{\vec{u}}_j = \vec{e}_3 \hat{\vec{\gamma}}_0^T \cdot (\hat{\vec{X}}_j - \hat{\vec{X}}_1) - \tfrac{1}{2} \vec{e}_3 \boldsymbol{\mathcal{K}}_0 : (\hat{\vec{X}}_j \hat{\vec{X}}_j - \hat{\vec{X}}_1 \hat{\vec{X}}_1) \qquad j = 1, 2, 3, 4 \tag{4.13}$$

The generalized periodicity constraints in the transverse direction (3.29) also reflect a linear relation between the displacement of two points on opposing boundaries. In contrast to the in-plane periodicity constraints (4.5),which are linear in η, the transverse periodicity constraints are linear in $\varsigma_1 = \frac{2X_1}{W}$ and $\varsigma_2 = \frac{2X_2}{T}$. The constraints (3.29) are recast in terms of transverse displacements as

$$\begin{aligned}
\tilde{\vec{u}}_{\mathrm{R}} &= \tilde{\vec{u}}_{\mathrm{L}} + \tfrac{1}{2}(1 - \varsigma_2)(\tilde{\vec{u}}_2 - \tilde{\vec{u}}_1) + \tfrac{1}{2}(1 + \varsigma_2)(\tilde{\vec{u}}_3 - \tilde{\vec{u}}_4) \\
\tilde{\vec{u}}_{\mathrm{F}} &= \tilde{\vec{u}}_{\mathrm{B}} + \tfrac{1}{2}(1 - \varsigma_1)(\tilde{\vec{u}}_4 - \tilde{\vec{u}}_1) + \tfrac{1}{2}(1 + \varsigma_1)(\tilde{\vec{u}}_3 - \tilde{\vec{u}}_2) \\
\tilde{\vec{u}}_{\mathrm{RF}} &= \tilde{\vec{u}}_{\mathrm{LB}} + 2\tilde{\vec{u}}_3 - \tilde{\vec{u}}_2 - \tilde{\vec{u}}_4
\end{aligned} \tag{4.14}$$

4.2 Micro to macro scale transition

After the analysis of a microstructural RVE is completed, the RVE averaged stress resultants are extracted and transported to the macroscopic level as the macroscopic stress resultants in the integration point. Of course, the stress resultants can be calculated by numerically evaluating the volume or surface integrals given in Section 3.2.2 and 3.3.2 for, respectively ,the Kirchhoff-Love and Mindlin-Reissner shell-types. However, for the particular implementation proposed here, computationally more efficient formulas may be obtained. The calculation of the stress resultant of the Kirchhoff-Love and Mindlin-Reissner shell-types are presented in the Sections 4.2.1 and 4.2.2, respectively.

For the finite element solution of the macroscopic problem a stiffness matrix at every macroscopic integration point is required. In computational homogenization schemes there is no explicit form of the macroscopic constitutive behaviour assumed a priori. Therefore the tangent operator has to be determined numerically. The higher-order computational homogenization scheme [5, 7] employs the direct condensation of the constrained degrees of freedom. The latter procedure can be used to derive the constitutive tangents for the shell-type continua. The calculation of the macroscopic stiffness matrices of the Kirchhoff-Love and Mindlin-Reissner shell-types are presented in the Sections 4.2.1 and 4.2.2, respectively.

4.2.1 Scale transition for a Kirchhoff-Love shell-type

The stress resultants (KL)

It may be verified that all forces involved in the homogeneous kinematic constraints (4.5) cancel out from the surface integrals in (3.17) and (3.18), while the forces involved in the non-homogeneous constraints (4.4) and (4.6), and the reaction forces at the prescribed corner nodes (4.3) have to be properly accounted for. From a balance of forces on the RVE, it can be shown the forces at the corner node 1 in the transverse direction is zero. After somewhat lengthy but straightforward mathematical manipulations the surface integrals (3.17) and (3.18) can be transformed into

$$\mathbf{N}_0 = \frac{1}{A_0}\sum_i \hat{\vec{f}}_{(i)}\hat{\vec{X}}^{\star}_{(i)}, \qquad i = 1,2,4,\widehat{56},\widehat{58},\mathrm{L}^*,\mathrm{B}^* \tag{4.15}$$

$$\mathbf{M}_0 = \frac{1}{A_0}\sum_i \hat{\vec{f}}_{(i)}\hat{\vec{Y}}^{\star}_{(i)}, \qquad i = 1,2,4,\widehat{56},\widehat{58},\mathrm{L}^*,\mathrm{B}^* \tag{4.16}$$

with

$$\hat{\vec{X}}^{\star}_i = \begin{cases} \hat{\vec{X}}_{(i)} - \hat{\vec{X}}_{(1)}, & \text{for } i = 1,2,4 \\ \hat{\vec{X}}_{(k)} - \hat{\vec{X}}_{(5)}, & \text{for } i = \widehat{56}(k=6), \widehat{58}(k=8) \\ \int_{\Gamma_{0\mathrm{L}}}(\hat{\vec{X}}_{\mathrm{L}} - \hat{\vec{X}}_{(1)})\mathrm{d}\Gamma_0, & \text{for } i = \mathrm{L}^* \\ \int_{\Gamma_{0\mathrm{B}}}(\hat{\vec{X}}_{\mathrm{B}} - \hat{\vec{X}}_{(1)})\mathrm{d}\Gamma_0, & \text{for } i = \mathrm{B}^* \end{cases} \tag{4.17}$$

$$\hat{\vec{Y}}^{\star}_i = \begin{cases} \zeta_{(1)}(\hat{\vec{X}}_{(i)} - \hat{\vec{X}}_{(1)}), & \text{for } i = 1,2,4 \\ \zeta_{(5)}(\hat{\vec{X}}_{(k)} - \hat{\vec{X}}_{(5)}), & \text{for } i = \widehat{56}(k=6), \widehat{58}(k=8) \\ \int_{\Gamma_{0\mathrm{L}}}(\zeta_{\mathrm{L}}\hat{\vec{X}}_{\mathrm{L}} - \zeta_{(1)}\hat{\vec{X}}_{(1)})\mathrm{d}\Gamma_0, & \text{for } i = \mathrm{L}^* \\ \int_{\Gamma_{0\mathrm{B}}}(\zeta_{\mathrm{B}}\hat{\vec{X}}_{\mathrm{B}} - \zeta_{(1)}\hat{\vec{X}}_{(1)})\mathrm{d}\Gamma_0, & \text{for } i = \mathrm{B}^* \end{cases} \tag{4.18}$$

In (4.15) and (4.16) $\hat{\vec{f}}_{(i)}$, i=1,2,4 are the in-plane reaction forces in the three prescribed corner nodes and $\hat{\vec{f}}_{\widehat{56}}$, $\hat{\vec{f}}_{\widehat{58}}$, $\hat{\vec{f}}_{\mathrm{L}^*}$, and $\hat{\vec{f}}_{\mathrm{B}^*}$ are the resultant forces necessary to enforce the non-homogeneous constraints (4.4) and (4.6). In a finite element program the forces $\hat{\vec{f}}_{(i)}$, $i = 1, 2, 4, \widehat{56}, \widehat{58}, \mathrm{L}^*, \mathrm{B}^*$ are readily available for the converged solution, from which the macroscopic stress resultants tensor $\mathbf{N}_0$ and the couple-stress resultant tensor $\mathbf{M}_0$ can be efficiently calculated using the formulas (4.15) and (4.16). Note that the RVE problem is a three-dimensional continuum problem and therefore in a standard implementation only the displacement degrees of freedom are unknown, this is contrast to a shell implementation, where typically also the rotations are unknown.

Macroscopic constitutive tangents (KL)

Procedures for imposing the homogeneous and non-homogeneous tyings, include the direct elimination of the dependent degrees of freedom from the system of equations, or the use of Lagrange multipliers of penalty functions. In this research, the constraints are enforced by elimination of the degrees of freedom for which a procedure is described in [7]. The prescribed degrees of freedom (among which are the prescribed displacements of the corner nodes and the non-homogeneous terms of constraints (4.4) and (4.6)) can be further eliminated from the system, leaving the displacements of the independent nodes as the only unknowns in the system.

The microscopic system of equation from which the dependent degrees of freedom have been eliminated is written as $\underline{K}\delta\underline{u} = \delta\underset{\sim}{f}^{\star}$ and rearranged to the form

$$\begin{bmatrix} \underline{K}_{pp} & \underline{K}_{pf} \\ \underline{K}_{fp} & \underline{K}_{ff} \end{bmatrix} \begin{bmatrix} \delta\underline{u}_p \\ \delta\underline{u}_f \end{bmatrix} = \begin{bmatrix} \delta\underline{f}_p \\ \delta\underline{f}_f \end{bmatrix} \approx \begin{bmatrix} \delta\underline{f}_p \\ \underline{0} \end{bmatrix} \tag{4.19}$$

where the subscript p refers to "prescribed" degrees of freedom (degrees of freedom through which the macroscopic generalized strain tensors are imposed on the RVE). The subscript f refers to all remaining "free" nodes. System (4.19) is taken at the converged end of a microscopic increment, thus the residual forces in the free nodes can be neglected $\delta\underline{f}_f \approx \underline{0}$. Elimination of $\delta\underline{u}_f$ form the system (4.19) leads to the reduces stiffness matrix $\underline{K}^{\star}$ that relates the variations of the prescribed degrees of freedom to the variations of the associated forces

$$\underline{K}^{\star}\delta\underline{u}_p = \delta\underline{f}_p, \qquad \text{with} \qquad \underline{K}^{\star} = \underline{K}_{pp} - \underline{K}_{pf}(\underline{K}_{ff})^{-1}\underline{K}_{fp}. \tag{4.20}$$

Next, relation (4.20) needs to be transformed to obtain an expression relating variations of the macroscopic stress resultant tensors to variations of the associated kinematical quantities. The linearized constitutive relations which are consistent with the macroscopic framework used for the Kirchhoff-Love shell description can be written as

$$\delta\mathbf{N}_0 = {}^4\mathbf{C}^{(1)} : \delta\boldsymbol{\mathcal{E}}_0^c + {}^4\mathbf{C}^{(2)} : \delta\boldsymbol{\mathcal{K}}_0^c \tag{4.21}$$

$$\delta\mathbf{M}_0 = {}^4\mathbf{C}^{(4)} : \delta\boldsymbol{\mathcal{E}}_0^c + {}^4\mathbf{C}^{(5)} : \delta\boldsymbol{\mathcal{K}}_0^c \tag{4.22}$$

where the fourth-order tensors ${}^4\mathbf{C}^{(1)}$, ${}^4\mathbf{C}^{(2)}$, ${}^4\mathbf{C}^{(3)}$, and ${}^4\mathbf{C}^{(5)}$ are the (yet unknown) macroscopic constitutive tangents. In order to obtain these constitutive tangents departing from the reduced matrix $\underline{K}^{\star}$, relation (4.20) is first rewritten in an in-plane vector/tensor format (note

that all the prescribed displacements leading to a non-zero reaction forces are the in-plane displacements and that all non-zero reaction forces have only in-plane components)

$$\sum_n \hat{\hat{\mathbf{K}}}^{\star}_{(in)} \cdot \delta\hat{\vec{u}}_{(n)} \;=\; \delta\hat{\vec{f}}_{(i)} \tag{4.23}$$

with $i, n = 1, 2, 4, \widehat{56}, \widehat{58}, \mathrm{L}^*, \mathrm{B}^*$, where the components of tensor $\hat{\hat{\mathbf{K}}}^{\star}_{(in)}$ are simply found in the tangent matrix $\underline{K}^{\star}$ at the rows and columns of the degrees of freedom corresponding to i and n. Next, the expression for the variation of forces (4.23) is substituted into the relations for the variation of the macroscopic stress and coupled stress obtained by varying (4.15) and (4.16), which lead to

$$\delta\mathbf{N}_0 \;=\; \frac{1}{A_0}\sum_i\sum_n (\hat{\hat{\mathbf{K}}}^{\star}_{(in)} \cdot \delta\hat{\vec{u}}_{(n)})\hat{\vec{X}}^{\star}_{(i)} \tag{4.24}$$

$$\delta\mathbf{M}_0 \;=\; \frac{1}{A_0}\sum_i\sum_n (\hat{\hat{\mathbf{K}}}^{\star}_{(in)} \cdot \delta\hat{\vec{u}}_{(n)})\hat{\vec{Y}}^{\star}_{(i)} \tag{4.25}$$

The vector $\delta\hat{\vec{u}}_{(n)}$ are now obtained form (4.3), (eq:disph568), and (4.7) as

$$\delta\hat{\vec{u}}_{(n)} \;=\; \hat{\vec{X}}^{\star}_{(n)} \cdot \delta\boldsymbol{\mathcal{E}}^c_0 + \hat{\vec{Y}}^{\star}_{(n)} \cdot \delta\boldsymbol{\mathcal{K}}^c_0 \tag{4.26}$$

Substitution of (4.26) into (4.24) and (4.25) gives

$$\delta\mathbf{N}_0 \;=\; \frac{1}{A_0}\sum_i\sum_n \left\{ \left(\hat{\vec{X}}^{\star}_{(i)}\hat{\hat{\mathbf{K}}}^{\star}_{(in)}\hat{\vec{X}}^{\star}_{(n)}\right)^{LC} : \delta\boldsymbol{\mathcal{E}}^c_0 + \left(\hat{\vec{X}}^{\star}_{(i)}\hat{\hat{\mathbf{K}}}^{\star}_{(in)}\hat{\vec{Y}}^{\star}_{(n)}\right)^{LC} : \delta\boldsymbol{\mathcal{K}}^c_0 \right\} \tag{4.27}$$

$$\delta\mathbf{M}_0 \;=\; \frac{1}{A_0}\sum_i\sum_n \left\{ \left(\hat{\vec{Y}}^{\star}_{(i)}\hat{\hat{\mathbf{K}}}^{\star}_{(in)}\hat{\vec{X}}^{\star}_{(n)}\right)^{LC} : \delta\boldsymbol{\mathcal{E}}^c_0 + \left(\hat{\vec{Y}}^{\star}_{(i)}\hat{\hat{\mathbf{K}}}^{\star}_{(in)}\hat{\vec{Y}}^{\star}_{(n)}\right)^{LC} : \delta\boldsymbol{\mathcal{K}}^c_0 \right\} \tag{4.28}$$

where the superscript LC indicates left conjugation, i.e. $T^{LC}_{ijkl} = T_{jikl}$. Comparing (4.27) and (4.28) with (4.21) and (4.22), the consistent tangents are finally identified as

$${}^4\mathbf{C}^{(1)} \;=\; \frac{1}{A_0}\sum_i\sum_n \left(\hat{\vec{X}}^{\star}_{(i)}\hat{\hat{\mathbf{K}}}^{\star}_{(in)}\hat{\vec{X}}^{\star}_{(n)}\right)^{LC} \tag{4.29}$$

$${}^4\mathbf{C}^{(2)} \;=\; \frac{1}{A_0}\sum_i\sum_n \left(\hat{\vec{X}}^{\star}_{(i)}\hat{\hat{\mathbf{K}}}^{\star}_{(in)}\hat{\vec{Y}}^{\star}_{(n)}\right)^{LC} \tag{4.30}$$

$${}^4\mathbf{C}^{(4)} \;=\; \frac{1}{A_0}\sum_i\sum_n \left(\hat{\vec{Y}}^{\star}_{(i)}\hat{\hat{\mathbf{K}}}^{\star}_{(in)}\hat{\vec{X}}^{\star}_{(n)}\right)^{LC} \tag{4.31}$$

$${}^4\mathbf{C}^{(5)} \;=\; \frac{1}{A_0}\sum_i\sum_n \left(\hat{\vec{Y}}^{\star}_{(i)}\hat{\hat{\mathbf{K}}}^{\star}_{(in)}\hat{\vec{Y}}^{\star}_{(n)}\right)^{LC} \tag{4.32}$$

Thus, the constitutive tangents of the macroscopic shell-type continuum are directly obtained through static condensation of the global microscopic (RVE) stiffness matrix. Notice that consistency is preserved through this micro-macro transition (provided that the consistent tangent operator is used at the microscale). In a geometrically non-linear case the obtained macroscopic tangents automatically include both geometrical and material contributions, evidently assuming that these parts have been properly dealt with on the microlevel [7].

4.2.2 Scale transition for a Mindlin-Reissner shell-type

The stress resultants (MR)

The same procedure used for the calculation of the stress resultants for the Kirchhoff-Love type shell are now used for the Mindlin-Reissner shell-type. Again, all the homogeneous constraint relations (4.5) and (4.14) satisfy the condition of zero virtual work and all the forces involved cancel out in the surface integrals (3.32), (3.33), (3.36). The stress resultants can be calculated from quantities related to the non-homogeneous terms in the constraints (4.4) and (4.11) and the prescribed corner nodes (4.10), and (4.13). The boundary integrals (3.32), (3.33), (3.36), which define the stress resultant of a Mindlin-Reissner shell, are transformed into

$$\mathbf{N}_0 = \frac{1}{A_0}\sum_i \hat{\vec{f}}_{(i)}\hat{\vec{X}}^\star_{(i)} \tag{4.33}$$

$$\mathbf{M}_0 = \frac{1}{A_0}\sum_i \hat{\vec{f}}_{(i)}\hat{\vec{Y}}^\star_{(i)} - \frac{1}{2A_0}\sum_j \vec{e}_3 \cdot \tilde{\vec{f}}_{(j)}\hat{\mathbf{Y}}^\star_{(j)}, \tag{4.34}$$

$$\hat{\vec{Q}}_0 = \frac{1}{2A_0}\sum_i \zeta^\star_{(i)}\hat{\vec{f}}_{(i)} + \frac{1}{2A_0}\sum_j \vec{e}_3 \cdot \tilde{\vec{f}}_{(j)}\hat{\vec{Z}}^\star_{(j)} \tag{4.35}$$

here and in the remainder of this section, quantities related to in-plane prescribed degrees of freedom are denoted by the indices $i, n = 1, 2, 4, \widehat{56}, \widehat{58}, \mathrm{L}^{**}, \mathrm{B}^{**}$ and quantities related to out-of-plane prescribed degrees of freedom are denoted by $j, m = 1, 2, 3, 4$. The "generalized" coordinates of these terms are

$$\hat{X}^\star_i = \begin{cases} \hat{\vec{X}}_{(i)} - \hat{\vec{X}}_{(1)}, & \text{for } i = 1, 2, 4 \\ \hat{\vec{X}}_{(k)} - \hat{\vec{X}}_{(5)}, & \text{for } i = \widehat{56}(k=6), \widehat{58}(k=8) \\ \int_{\Gamma_{0\mathrm{L}}} \zeta_\mathrm{L}(\hat{\vec{X}}_\mathrm{L} - \hat{\vec{X}}_{(1)})\mathrm{d}\Gamma_0, & \text{for } i = \mathrm{L}^{**} \\ \int_{\Gamma_{0\mathrm{B}}} \zeta_\mathrm{B}(\hat{\vec{X}}_\mathrm{B} - \hat{\vec{X}}_{(1)})\mathrm{d}\Gamma_0, & \text{for } i = \mathrm{B}^{**} \end{cases} \tag{4.36}$$

$$\hat{Y}^\star_i = \begin{cases} \zeta_{(1)}(\hat{\vec{X}}_{(i)} - \hat{\vec{X}}_{(1)}), & \text{for } i = 1, 2, 4 \\ \zeta_{(5)}(\hat{\vec{X}}_{(k)} - \hat{\vec{X}}_{(5)}), & \text{for } i = \widehat{56}(k=6), \widehat{58}(k=8) \\ \int_{\Gamma_{0\mathrm{L}}} \zeta_\mathrm{L}(\zeta_\mathrm{L}\hat{\vec{X}}_\mathrm{L} - \zeta_{(1)}\hat{\vec{X}}_{(1)})\mathrm{d}\Gamma_0, & \text{for } i = \mathrm{L}^{**} \\ \int_{\Gamma_{0\mathrm{B}}} \zeta_\mathrm{B}(\zeta_\mathrm{B}\hat{\vec{X}}_\mathrm{B} - \zeta_{(1)}\hat{\vec{X}}_{(1)})\mathrm{d}\Gamma_0, & \text{for } i = \mathrm{B}^{**} \end{cases} \tag{4.37}$$

$$\zeta^\star_i = \begin{cases} \zeta_{(i)} - \zeta_{(1)}, & \text{for } i = 1, 2, 4 \\ \zeta_{(k)} - \zeta_{(5)}, & \text{for } i = \widehat{56}(k=6), \widehat{58}(k=8) \\ \int_{\Gamma_{0\mathrm{L}}} \zeta_\mathrm{L}(\zeta_\mathrm{L} - \zeta_{(1)})\mathrm{d}\Gamma_0, & \text{for } i = \mathrm{L}^{**} \\ \int_{\Gamma_{0\mathrm{B}}} \zeta_\mathrm{B}(\zeta_\mathrm{B} - \zeta_{(1)})\mathrm{d}\Gamma_0, & \text{for } i = \mathrm{B}^{**} \end{cases} \tag{4.38}$$

$$\hat{\mathbf{Y}}^\star_j = \left\{ \hat{\vec{X}}_{(j)}\hat{\vec{X}}_{(j)} - \hat{\vec{X}}_{(1)}\hat{\vec{X}}_{(1)}, \quad \text{for } j = 1, 2, 3, 4 \right. \tag{4.39}$$

$$\hat{\vec{Z}}^\star_j = \left\{ \hat{\vec{X}}_{(j)} - \hat{\vec{X}}_{(1)}, \quad \text{for } j = 1, 2, 3, 4 \right. \tag{4.40}$$

Macroscopic constitutive tangents (MR)

Similar as for the Kirchhoff-Love shell-type continuum, here the consistent tangents are obtained by condensation of the microstructural RVE stiffness matrix in the converged configu-

ration. The linearized macroscopic constitutive equations of the Mindlin-Reissner shell-type are written in a general form as

$$\delta\mathbf{N}_0 = {}^4\mathbf{C}^{(1)} : \delta\boldsymbol{\mathcal{E}}_0^c + {}^4\mathbf{C}^{(2)} : \delta\boldsymbol{\mathcal{K}}_0^c + {}^3\mathbf{C}^{(3)} \cdot \delta\hat{\vec{\gamma}}_0 \tag{4.41}$$

$$\delta\mathbf{M}_0 = {}^4\mathbf{C}^{(4)} : \delta\boldsymbol{\mathcal{E}}_0^c + {}^4\mathbf{C}^{(5)} : \delta\boldsymbol{\mathcal{K}}_0^c + {}^3\mathbf{C}^{(6)} \cdot \delta\hat{\vec{\gamma}}_0 \tag{4.42}$$

$$\delta\hat{\vec{Q}}_0 = {}^3\mathbf{C}^{(7)} : \delta\boldsymbol{\mathcal{E}}_0^c + {}^3\mathbf{C}^{(8)} : \delta\boldsymbol{\mathcal{K}}_0^c + {}^2\mathbf{C}^{(9)} \cdot \delta\hat{\vec{\gamma}}_0 \tag{4.43}$$

The reduced matrix $\underline{K}^\star$ of equation (4.20) is written in a vector/tensor format and splitted into the parts related to the in-plane and out-of-plane prescribed degrees of freedom $\hat{\mathbf{K}}^\star_{(in)}$, $\hat{\tilde{\mathbf{K}}}^\star_{(im)}$, $\tilde{\hat{\mathbf{K}}}^\star_{(jn)}$, and $\tilde{\tilde{\mathbf{K}}}^\star_{(jm)}$

$$\sum_n \hat{\mathbf{K}}^\star_{(in)} \cdot \delta\hat{\vec{u}}_{(n)} + \sum_m \hat{\tilde{\mathbf{K}}}^\star_{(im)} \cdot \delta\tilde{\vec{u}}_{(m)} = \delta\hat{\vec{f}}_{(i)} \tag{4.44}$$

$$\sum_n \tilde{\hat{\mathbf{K}}}^\star_{(jn)} \cdot \delta\hat{\vec{u}}_{(n)} + \sum_m \tilde{\tilde{\mathbf{K}}}^\star_{(jm)} \cdot \delta\tilde{\vec{u}}_{(m)} = \delta\tilde{\vec{f}}_{(j)} \tag{4.45}$$

Next, the expressions for the variations of forces (4.44) and (4.45) are substituted into the relations for the variations of the stress resultants obtained by varying (4.33), (4.34), and (4.35). The vectors $\delta\hat{\vec{u}}_{(n)}$ and $\delta\tilde{\vec{u}}_{(m)}$ are then replaced by the expressions obtained by variation of the in-plane degrees of freedom (4.10), (4.4), (4.12) and the out-of-plane degrees of freedom (4.13)

$$\delta\hat{\vec{u}}_{(n)} = \hat{\vec{X}}^\star_{(n)} \cdot \delta\boldsymbol{\mathcal{E}}_0^c + \hat{\vec{Y}}^\star_{(n)} \cdot \delta\boldsymbol{\mathcal{K}}_0^c + \zeta^\star_{(n)}\delta\hat{\vec{\gamma}}_0 \tag{4.46}$$

$$\delta\tilde{\vec{u}}_{(m)} = \hat{\vec{Z}}_{(m)} \cdot \delta\hat{\vec{\gamma}}_0^r\vec{e}_3 - \frac{1}{2}\hat{\mathbf{Y}}^\star_{(m)} : \delta\boldsymbol{\mathcal{K}}_0\vec{e}_3 \tag{4.47}$$

The recovered definitions of macroscopic constitutive stiffness tensors can be found in Appendix A.

Chapter 5

Comparative analyses

In the previous chapters the computational homogenization schemes for a Kirchhoff-Love and a Mindlin-Reissner shell-type continuum have been elaborated. In this chapter some illustrative examples are presented obtained using the two schemes. In the first section the homogenized response of a homogeneous and a structured microscale RVE under different prescribed macroscale deformation modes are discussed. The homogenized generalized stress-strain relation of homogeneous shells is compared to the stress-strain response of classical shells with a closed-form constitutive model. In Section 5.2 two examples of multi-scale analyses are given, one for a transversely loaded sheet, and one for a sheet subjected to a twisting loading.

5.1 Microstructural analyses

5.1.1 Homogeneous shell

First, the initial macroscopic stiffness tensors obtained from an RVE with homogeneous material properties are compared to the linear elastic stiffness tensors from classical shell theories. The macroscopic stiffness tensors relating generalized stress resultants and generalized strain tensors crosswise (${}^{4}\mathbf{C}^{(2)}$, ${}^{3}\mathbf{C}^{(3)}$, ${}^{4}\mathbf{C}^{(5)}$, ${}^{3}\mathbf{C}^{(6)}$, ${}^{3}\mathbf{C}^{(7)}$, and ${}^{3}\mathbf{C}^{(8)}$), as defined in Chapter 4 by relations (4.21), (4.22), (4.41)-(4.43), are initially zero. The obtained initial macroscopic stiffness tensors ${}^{4}\mathbf{C}^{(1)}$ and ${}^{4}\mathbf{C}^{(5)}$ condensed from the stiffness matrix of the RVE are similar for the homogenized Kirchhoff-Love and Mindlin-Reissner shell-type. Naturally, ${}^{4}\mathbf{C}^{(1)}$ and ${}^{4}\mathbf{C}^{(5)}$ are equal to the linear elastic stiffness tensors of the classical shell theories, here written in a matrix notation

$$\underline{C}^{(1)} = \frac{EH}{1-\nu^2}\begin{bmatrix} 1 & \nu & 0 \\ \nu & 1 & 0 \\ 0 & 0 & (1-\nu)/2 \end{bmatrix}, \qquad \underline{C}^{(5)} = \frac{H^2}{12}\underline{C}^{(1)} \tag{5.1}$$

According to the Mindlin-Reissner shell theory, the elastic transverse shear stiffness tensor ${}^{2}\mathbf{C}^{(9)}$ (see (4.43)) of a homogeneous shell, for which the transverse shear is assumed to be quadratic through its thickness, equals to $\frac{5}{6}G\hat{\hat{\mathbf{I}}}$, where G is the shear modulus. Figure 5.1 shows the initial transverse shear stiffness obtained from homogeneous RVEs with different ratios of RVE width W (depth of the RVE $W = D$) and thickness H. The stiffness depicted is relative to the stiffness resulting from true parabolic transverse shear. The transverse shear

stiffness decreases with increasing W/H-ratio. In 5.1(a)-(c) the deformed RVEs corresponding to the W/H-ratios of points (a)-(c) in graph of Figure 5.1 are shown. It shows that for larger in-plane size of the RVE, the RVE will respond to the imposed transverse shear by a s-shaped curvature. This result is not surprising, since as has been discussed in Section 3.3.1, the macro-micro transition for the transverse shear along a fiber (3.23) has been applied to the RVE transverse boundaries vice (3.24) therefore, the wider the RVE, the larger the difference between the transverse shear response of the finite size RVE and the fiber.

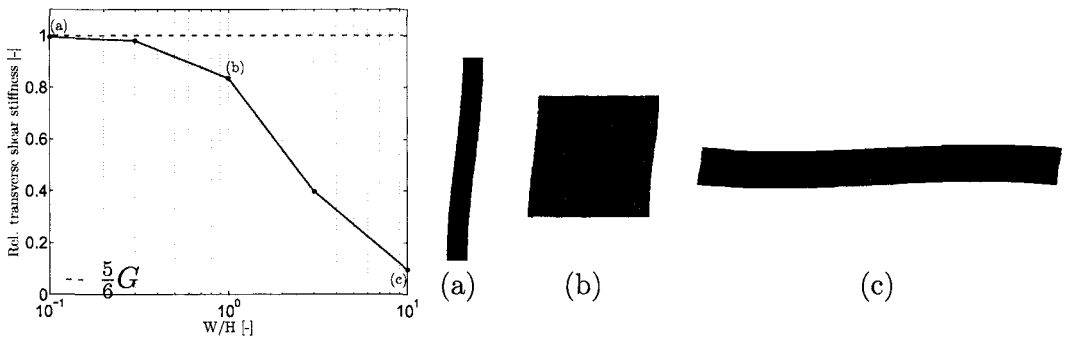

Figure 5.1: The relative transverse shear stiffness as a function of the W/H-ratio of the RVE, (a)-(c) show deformed RVEs of different W/H-ratio to which pure transverse shear was prescribed

In the next test, a three-dimensional initially square homogeneous RVE was used with dimensions $W = T = H = 1$mm. The mesh consists of $6 \times 6 \times 6$ solid 20-node elements. A standard elasto-plastic Von Mises model is used for the material behaviour, with Young's modulus $E = 210$kPa, a Poisson's ratio $\nu = 0.3$, a yield stress $\sigma_y = 1.0$kPa and a linear hardening with modulus $h = 52.5$kPa. The non-zero generalized stress resultants obtained through the homogenization of the RVE are visualized in Figure 5.2 for the different prescribed macroscopic deformation modes. The solid lines in Figure 5.2 represent the responses from the homogenized RVE for a Mindlin-Reissner type-RVEs. The homogenized responses obtained from a Kirchhoff-Love type-RVE are comparable to Figure 5.2(a)-(d). The dots represent the generalized stress resultants from classical Mindlin-Reissner shell theory. The thickness of the classical shell is assumed to be constant, whereas the thickness of the RVE is free to decrease for large in-plane strains. This causes a small difference between the response of the homogenized RVE and the response of the classical shell, this difference is just slightly visible in Figure 5.2.a. The transition of the elastic to the elasto-plastic regime for the bending (Fig. 5.2.c) and twisting (Fig. 5.2.d) modes also differs from the classical shell response with respect to the homogenized response. In Figure 5.2e the response to a prescribed transverse shear is depicted. The solid line represents the initially square RVE which corresponds to point (b) in Figure 5.1. The dots represent the response of a classical Mindlin-Reissner shell, for which a constant through-thickness transverse shear is assumed, i.e. ${}^2\mathbf{C}^{(9)} = G\hat{\hat{\mathbf{I}}}$. The dotted gray line represent the response of a linear elastic shell with parabolic transverse shear, i.e. ${}^2\mathbf{C}^{(9)} = \frac{5}{6}G\hat{\hat{\mathbf{I}}}$.

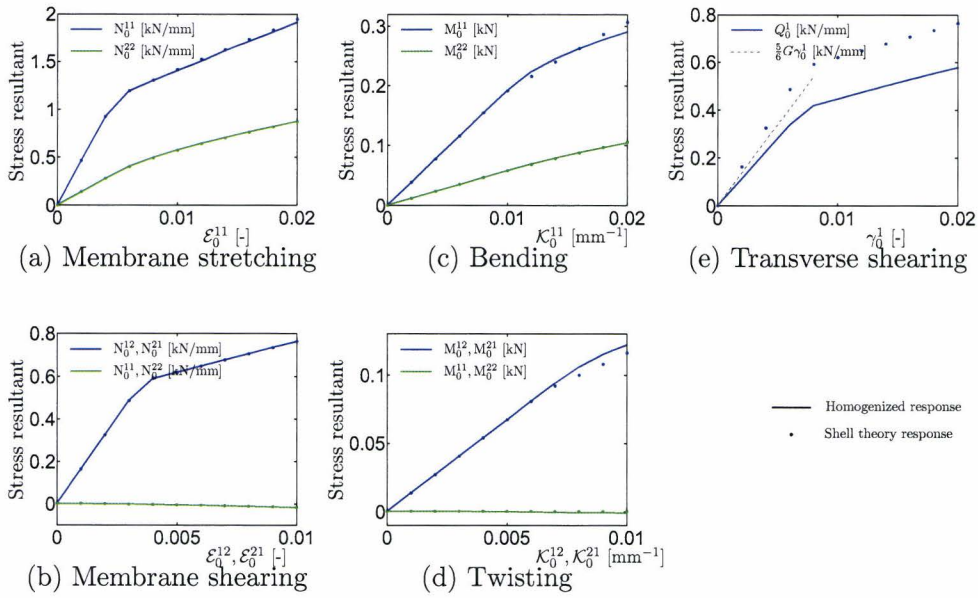

Figure 5.2: Macroscopic response for different RVE deformation modes of a homogeneous elasto-plastic Mindlin-Reissner RVE

5.1.2 Substructured shell

A periodic structure is considered to be represented by cubic 3D RVEs with a complex through-thickness substructure, see Figure 5.3, composed of elastic and elasto-plastic von Mises (with linear hardening) materials. The material parameters of different materials comprising the structure are also given in Figure 5.3.

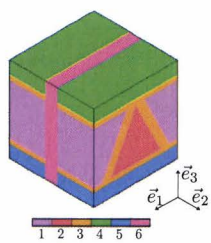

Material	E (kPa)	ν	σ_y (kPa)	h (kPa)
1,2	2.0	0.42	-	-
3	210	0.3	0.51	0.2
4,5	30	0.4	0.6	5
6	10	0.15	-	-

Figure 5.3: Through-thickness 3D RVE, substructured with 6 materials

Figure 5.4 shows the deformed RVEs, with the contour plots of the equivalent von Mises stress, obtained by applying different macroscopic deformation modes. Note the pronounced heterogeneous stress field distribution throughout the different layers for the different loading cases, which cannot be captured in a closed-form homogenization of the RVE response nor by the layer-wise homogenization. In Figure 5.5 the homogenized non-zero generalized stress resultants corresponding to the different RVE deformation modes shown in Figure 5.4 are given.

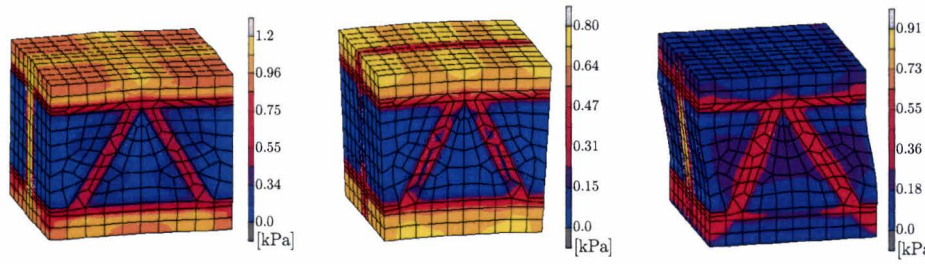

(a) Membrane stretching (c) Bending (e) Transverse shearing

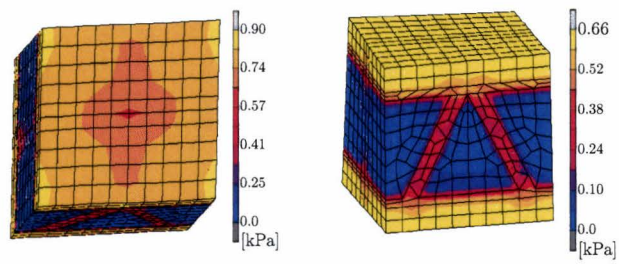

(b) Membrane shearing (d) Twisting

Figure 5.4: RVE deformation modes and the distribution of the equivalent von Mises stress

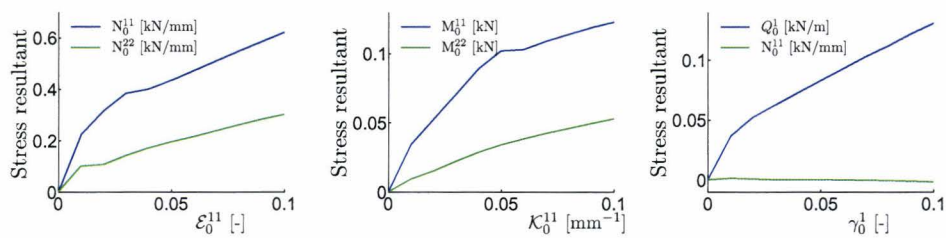

(a) Membrane stretching (c) Bending (e) Transverse shearing

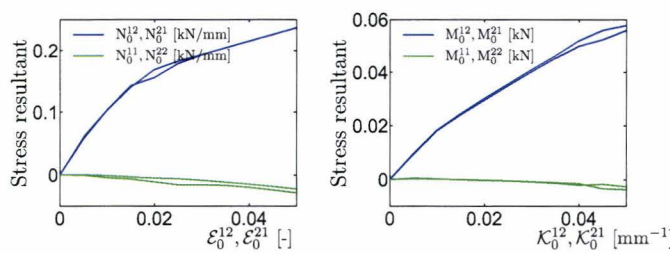

(b) Membrane shearing (d) Twisting

Figure 5.5: Macroscopic homogenized response of the heterogeneous Mindlin-Reissner RVE for difference RVE deformation modes (only components of the stress resultants significantly different from zero are shown for each loading case)

5.2 Multi-scale analyses

5.2.1 Transversely loaded sheet

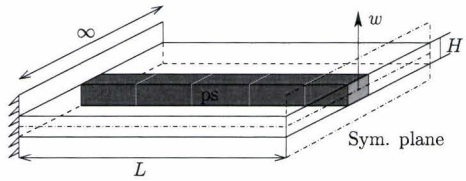

Figure 5.6: Schematic representation of a shell with a typical plane strain loading, which is clamped on one end and has a symmetry plane on the other

In the first multi-scale analysis example a shell with thickness $H = 1\text{mm}$ is considered that is clamped on the two ends and in the center a vertical displacement w is prescribed. Because of the symmetry, only the left-hand side of the shell is modelled, see Figure 5.6. The length L of half the shell is 50mm and the other in-plane dimension is very large compared to that. Therefore, only a narrow strip of the shell needs to be modelled and the plane strain conditions (ps) are prescribed to the strip edges. The multi-scale problem is solved with 5 Kirchhoff-Love or Mindlin-Reissner shell elements only, see Figure 5.6. The Kirchhoff-Love shell element has 4-nodes with global displacements and rotations as degrees of freedom. Bilinear interpolation is used for the coordinates, displacements and rotations. The membrane strains are obtained from the displacement field; the curvatures from the rotation field. The description of Mindlin-Reissner elements is similar and the transverse shear strains are calculated at the middle of the edges and interpolated to the integration points points. In this way, this element behaves correctly in the limiting case of thin shells [9].

Three different microstructures are attributed to the shell, type (i) is homogeneous elastic with Young's modulus $E = 210\text{kPa}$ and Poisson's ratio $\nu = 0.3$, type (ii) is homogeneous elasto-plastic with the same elastic properties and a yield stress of $\sigma_y = 1.0\text{kPa}$ and linear hardening modulus $h = 52.5\text{kPa}$, and type (iii) a substructured shell for which the microstructure is defined in Figure 5.3.

Figure 5.7b shows the force per unit length in the out-of-plane direction F_3' as a function of the prescribed displacement w for shell of type (i). The red line is the reference solution obtained from a full-scale 3D continuum modelling of the shell. The blue and green line represent the multi-scale solutions obtained from Kirchhoff-Love and Mindlin-Reissner shell-type element, respectively. The comparison of the global response of the Mindlin-Reissner element and the reference solution is very good. The response of the multi-scale Kirchhoff-Love solution is somewhat stiffer then the reference solution. In Figure 5.7a the deformed profiles of the Kirchhoff-Love (blue) and the Mindlin-Reissner (green) multi-scale shell are depicted. The deformed RVEs with contour plots of the equivalent Von Mises stress are shown for three places.

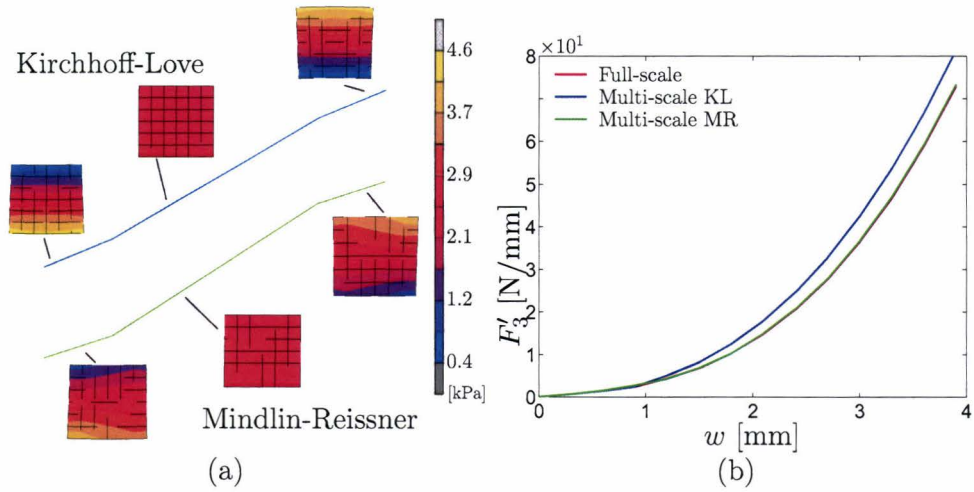

Figure 5.7: Multi-scale analysis of a transversely loaded homogeneous elastic shell; (a) the macroscopic deformed profiles and the associated RVEs with equivalent Von Mises contour plots; (b) the global response of a Kirchhoff-Love shell, a Mindlin-Reissner shell and a reference 3D full scale continuum model

To investigate the origin of the stiffer response of the homogenized Kirchhoff-Love shell, the values of the obtained generalized strains have to be compared. The membrane strain is constant throughout both the Kirchhoff-Love $\mathcal{E}^{11}_{KL} = 3.1 \cdot 10^{-3}$ and the Mindlin-Reissner $\mathcal{E}^{11}_{MR} = 3.3 \cdot 10^{-3}$ shells. The out-of-plane displacement of the Kirchhoff-Love shell is fully developed by bending with curvature $\mathcal{K}^{11}_{KL} = \pm 0.014 \text{mm}^{-1}$, while for the Mindlin-Reissner shell this is a combined contribution of bending $\mathcal{K}^{11}_{MR} = \pm 9.7 \cdot 10^{-3} \text{mm}^{-1}$ and a rather noticeable transverse shear strain $\gamma^{1}_{MR} = 0.65 \cdot 10^{-3}$. It shows the importants of transverse shear in areas with a large gradient of curvature.

Figure 5.8b shows the global response of a homogeneous elasto-plastic shell (type (ii)). The counter plots of the deformed RVEs in Figure 5.8a show the plastic strain energy density. Notice that the profile of the deformed KL-shell clearly differs from the deformed profile of the Mindlin-Reissner shell. Because of the the plastic deformation at the ends and at the symmetry plane of the shell, the membrane strain is no longer constant throughout the shell. Due to the plastic yielding, the deformation is more concentrated around the clamped end and the symmetry plane of the shell. The points y_{KL} and y_{MR} mark the points where the local plastic deformation within RVEs (at the end and at center of the shell) initiates for the Kirchhoff-Love and the Mindlin-Reissner shells, respectively. The lack of transverse shear strains becomes more prevalent in the global response of the Kirchhoff-Love shell after yielding in at these positions, see Figure 5.8b.

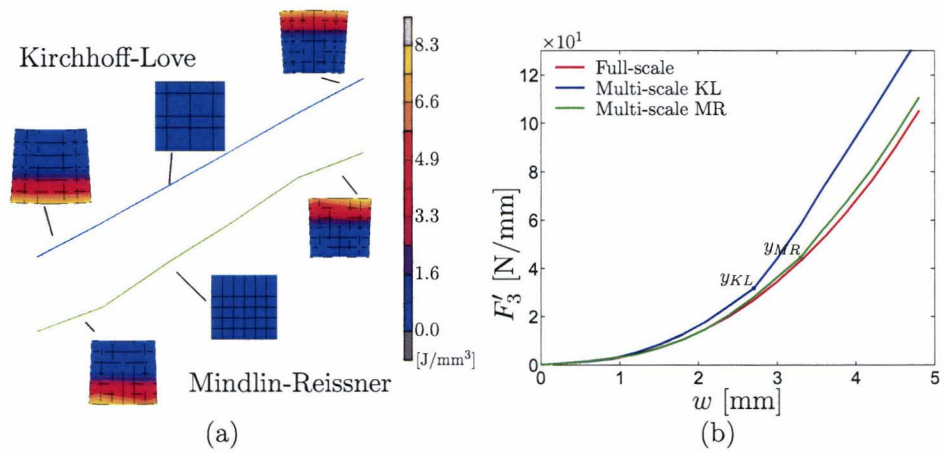

Figure 5.8: Multi-scale analysis of a transversely loaded homogeneous elastic-plastic shell; (a) the deformed macroscopic profiles and the associated RVEs with plastic strain energy density contour plots; (b) the global response of a Kirchhoff-Love shell, a Mindlin-Reissner shell and a reference 3D full scale continuum

Finally, the macroscopic shell depicted in Figure 5.6 in combination with the microstructure shown in Figure 5.3 is used (case(iii)). Figure 5.9 shows the macroscopic response of the shell for both the Kirchhoff-Love (blue) and Mindlin-Reissner (green) shell. No reference response is shown because the modelling of one row of 50 microstructural RVE to represent half of the shell, results in a prohibitively large mesh. The macroscopic response of the Mindlin-Reissner shell is relatively smooth, as expected. The response of the response of the Kirchhoff-Love shell shows jumps for the larger displacements. Probably, this is the result of a too large increment step size in the regions where macroscopic Gauss points go from the elastic to elasto-plastic regime. In Figure 5.10 the deformed profiles are shown accompanied by the deformed RVEs with equivalent von Mises contour plots for 3 different positions.

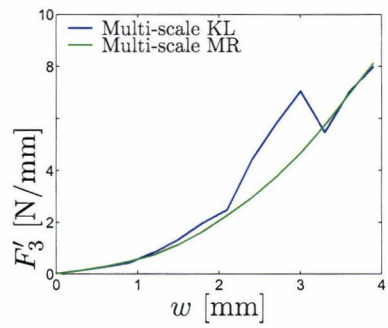

Figure 5.9: The global response of a Kirchhoff-Love shell and a Mindlin-Reissner shell obtained for a multi-scale analysis of a transversely loaded heterogeneous shell

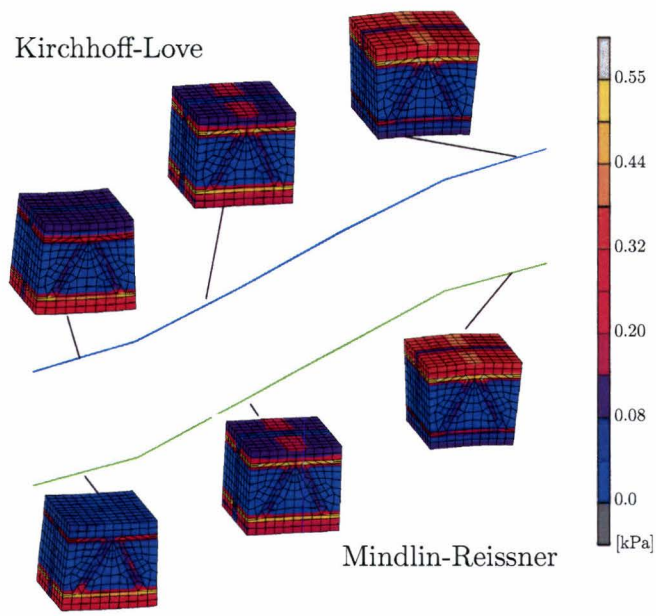

Figure 5.10: The macroscopic deformed profiles and associated RVEs with equivalent Von Mises contour plots obtained for a multi-scale analysis of a transversely loaded heterogeneous

5.2.2 Sheet with a twisting type of loading

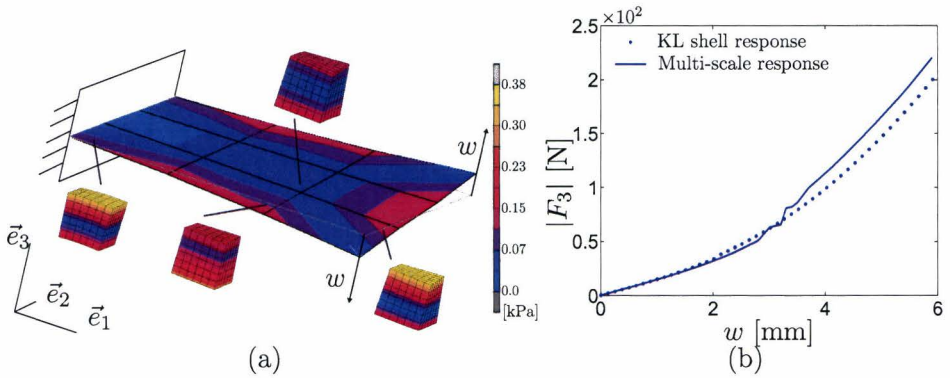

Figure 5.11: Multi-scale analysis of a homogeneous elasto-plastic shell with a twisting loading; (a) the deformed macroscopic mesh and associated RVEs of the Kirchhoff-Love shell; (b) the global response of a Kirchhoff-Love shell obtained by direct and multi-scale modelling

To demonstrate the capability of the proposed computational homogenization framework to perform a fully three-dimensional loading analysis, an initially flat square sheet with outer dimensions $L = 50$mm is clamped at on edge. To one corner a vertical displacement of w is prescribed and to the other corner the same displacement is prescribed in the opposite direction producing a twisting deformation at the plate, see Figure 5.11a. The sheet is modelled by 9 Kirchhoff-Love shell-elements and it has the homogeneous elasto-plastic proporties of case (ii). In Figure 5.11b the macroscopic response of the classical Kirchhoff-Love (dots) and the Kirchhoff-Love multi-scale (solid line) analyses are shown. The absolute reaction forces $|F_3|$ at the prescribed nodes is plotted again the prescribed displacement w. Again, there is a small region where the incremental step size apparently was too large to give a smooth response. The overall response of the multi-scale response differs slightly from the response of a direct analysis of the shell by a Kirchhoff-Love element, this was also shown in Figures 5.2c and 5.2d. In Figure 5.11a, the deformed sheet is shown accompanied by deformed microstructural RVE with Von Mises contour plots at some typically positions.

Chapter 6

Conclusions and recommendations

Shell-type continua with functional periodic microstructure may be found in various engineering applications. The development of these structures often calls for an analysis of the complex micro-macro structure-properties relations. The objective of this research is to develop a two-scale computational homogenization approach for structured thin sheets. Homogenization approaches avoid extensive experimental measuring and compared to direct modeling of the whole heterogeneous structure there is a large reduction in the number of degrees of freedom.

The computational homogenization technique is essentially based on the solution of two nested boundary value problems, one for each scale. No closed-form constitutive model needs to be chosen for the macrolevel, which makes the technique suitable to deal with complex loading and an evolving microstructure. Additionally, as has been demonstrated in this work, macroscopic constitutive tangent operators, necessary for the solution of the macroscopic problem within, for example, a finite element framework, can be obtained easily from the microscopic overall stiffness matrix by static condensation. Importantly, consistency is preserved through this scale transition.

In this work, the three dimensional macroscopic structure is modelled by a shell-type boundary value problem derived from a classical shell theory. The theories used in this research are the Kirchhoff-Love and the kinematically more rich Mindlin-Reissner theories, which were summarized in Chapter 2. Evidently, the choice of a shell theory has an influence on the precise scale transition relations, even though the application of the framework to other shell formulations (e.g. solid-like shell) can be readily obtained in a similar manner. Departing from assumptions of a shell theory an appropriate shell transition can be established to arrive at a consistent multi-scale computational homogenization framework. The shell formulation is used that assumes the curvatures and the transverse shear to be small relative to the shell thickness, while the large macroscopic displacements, rotations and membrane strains are possible.

The developed computational homogenization for structured thin sheets fits entirely in a standard shell mechanics framework. The computational homogenization scheme was presented in Chapter 3. Generalized strains describing the local membrane strains, curvatures and for Mindlin-Reissner shells transverse shears are calculated for every material point of the macrostructure (e.g. an integration point on the surface macromesh within a finite element environment). These generalized strains are used to formulated essential and natural boundary conditions to be imposed on the microstructural representative volume element that is

assigned to the macroscopic point. In the present framework, the three-dimensional RVE represents the full thickness and a periodic in-plane cell of the macroscopic structure.

Upon the solution of the microstructural boundary value problem, the macroscopic generalized stress resultants are obtained by averaging the resulting RVE stress field over the in-plane area of the microstructural cell. Hence, the stress integration through the thickness of the shell is combined with an in-plane homogenization. The generalized stress resultants represent forces and moments working on a line-element in the reference surface of the shell. From a macroscopic point of view, a (numerical) generalized stress-strain relationship at every macroscopic point is readily obtained. With a modified version of the Hill-Mandel energy condition it was shown that the generalized stress resultants defined in the computational homogenization scheme are consistent with the definitions used in shell theories.

In this research the emphasis has been on an initially three dimensional rectangular RVE that represents the underlying microstructure of an initially flat shell. The computational homogenization scheme for such a sheet has been implemented, for which details were discussed in Chapter 4. Finally, the homogenized response of a homogeneous RVE has been compared to the macrostructural response of the classical shell theories with closed-form elasto-plastic constitutive behaviour. Also, the homogenized response of a heterogeneous microstructure for different macroscopic deformation modes has been calculated. Two examples of multi-scale analyses are given, in one the macroscopic shell is meanly transversely loaded, while in the other the shell is subjected to a twisting loading.

The analysis of realistic applications requires a considerable computational effect, since both scales are numerically solved concurrently. The calculations times required can be reduced by the use of parallel computations. One of the possible parallel implementations schemes has been presented in [5]. Also, a different type (lower order) of solid element to model the microstructure could be used. Despite the required computational effort, the presented multi-scale computational homogenization procedure a very useful and powerful tool for the analysis of structured thin sheets with any, possible very complex, periodic microstructure.

Appendix A

Constitutive tensors (MR)

The constitutive macroscopic stiffness tensors for a homogenized Mindlin-Reissner shell defined by (4.33), (4.34), and (4.35) calculated directly from the reduced stiffness matrix that relates the variation of the prescribed degrees of freedom to the variations of the associated forces. Quantities related to in-plane prescribed degrees of freedom are denoted by the indices $i, n = 1, 2, 4, \widehat{56}, \widehat{58}, \mathrm{L}^{**}, \mathrm{B}^{**}$ and quantities related to out-of-plane prescribed degrees of freedom are denoted by $j, m = 1, 2, 3, 4$.

$$
{}^{4}\mathbf{C}^{(1)} = \frac{1}{A_0} \sum_i \sum_n \left(\hat{\vec{X}}^{\star}_{(i)} \hat{\mathbf{K}}^{\star}_{(in)} \hat{\vec{X}}^{\star}_{(n)} \right)^{LC} \tag{A.1}
$$

$$
{}^{4}\mathbf{C}^{(2)} = \frac{1}{A_0} \left\{ \sum_i \sum_n \left(\hat{\vec{X}}^{\star}_{(i)} \hat{\mathbf{K}}^{\star}_{(in)} \hat{\vec{Y}}^{\star}_{(n)} \right)^{LC} - \tfrac{1}{2} \sum_i \sum_m \left(\hat{\vec{X}}^{\star}_{(i)} \hat{\tilde{\mathbf{K}}}^{\star}_{(im)} \cdot \vec{e}_3 \hat{\mathbf{Y}}^{\star}_{(m)} \right)^{LC} \right\} \tag{A.2}
$$

$$
{}^{3}\mathbf{C}^{(3)} = \frac{1}{2A_0} \left\{ \sum_i \sum_n \left(\hat{\vec{X}}^{\star}_{(i)} \hat{\mathbf{K}}^{\star}_{(in)} \zeta^{\star}_{(n)} \right)^{LC} + \sum_i \sum_m \left(\hat{\vec{X}}^{\star}_{(i)} \hat{\tilde{\mathbf{K}}}^{\star}_{(im)} \cdot \vec{e}_3 \hat{\vec{Z}}^{\star}_{(m)} \right)^{LC} \right\} \tag{A.3}
$$

$$
{}^{4}\mathbf{C}^{(4)} = \frac{1}{A_0} \left\{ \sum_i \sum_n \left(\hat{\vec{Y}}^{\star}_{(i)} \hat{\mathbf{K}}^{\star}_{(in)} \hat{\vec{X}}^{\star}_{(n)} \right)^{LC} - \sum_j \sum_n \left(\hat{\mathbf{Y}}^{\star}_{(j)} \vec{e}_3 \cdot \hat{\tilde{\mathbf{K}}}^{\star}_{(jn)} \hat{\vec{X}}^{\star}_{(n)} \right) \right\} \tag{A.4}
$$

$$
\begin{aligned}
{}^{4}\mathbf{C}^{(5)} = \frac{1}{A_0} \Bigg\{ & \sum_i \sum_n \left(\hat{\vec{Y}}^{\star}_{(i)} \hat{\mathbf{K}}^{\star}_{(in)} \hat{\vec{Y}}^{\star}_{(n)} \right)^{LC} - \tfrac{1}{2} \sum_j \sum_n \left(\hat{\mathbf{Y}}^{\star}_{(j)} \vec{e}_3 \cdot \hat{\tilde{\mathbf{K}}}^{\star}_{(jn)} \hat{\vec{Y}}^{\star}_{(n)} \right) - \dots \\
& \tfrac{1}{2} \sum_i \sum_m \left(\hat{\vec{Y}}^{\star}_{(i)} \hat{\tilde{\mathbf{K}}}^{\star}_{(im)} \cdot \vec{e}_3 \hat{\mathbf{Y}}^{\star}_{(m)} \right)^{LC} + \tfrac{1}{4} \sum_j \sum_m \left(\hat{\mathbf{Y}}^{\star}_{(j)} \vec{e}_3 \cdot \hat{\tilde{\mathbf{K}}}^{\star}_{(jm)} \cdot \vec{e}_3 \hat{\mathbf{Y}}^{\star}_{(m)} \right) \Bigg\}
\end{aligned} \tag{A.5}
$$

$$
\begin{aligned}
{}^{3}\mathbf{C}^{(6)} = \frac{1}{2A_0} \Bigg\{ & \sum_i \sum_n \left(\hat{\vec{Y}}^{\star}_{(i)} \hat{\mathbf{K}}^{\star}_{(in)} \zeta^{\star}_{(n)} \right)^{LC} - \sum_j \sum_n \left(\hat{\mathbf{Y}}^{\star}_{(j)} \vec{e}_3 \cdot \hat{\tilde{\mathbf{K}}}^{\star}_{(jn)} \zeta^{\star}_{(n)} \right) + \dots \\
& \sum_i \sum_m \left(\hat{\vec{Y}}^{\star}_{(i)} \hat{\tilde{\mathbf{K}}}^{\star}_{(im)} \cdot \vec{e}_3 \hat{\vec{Z}}^{\star}_{(m)} \right)^{LC} - \sum_j \sum_m \left(\hat{\mathbf{Y}}^{\star}_{(j)} \vec{e}_3 \cdot \hat{\tilde{\mathbf{K}}}^{\star}_{(jm)} \cdot \vec{e}_3 \hat{\vec{Z}}^{\star}_{(m)} \right) \Bigg\}
\end{aligned} \tag{A.6}
$$

$$
{}^{3}\mathbf{C}^{(7)} = \frac{1}{2A_0}\left\{\sum_i\sum_n\left(\zeta^\star_{(i)}\hat{\tilde{\mathbf{K}}}^\star_{(in)}\hat{\tilde{X}}^\star_{(n)}\right)+\sum_j\sum_n\left(\hat{\tilde{Z}}^\star_{(j)}\vec{e}_3\cdot\tilde{\hat{\mathbf{K}}}^\star_{(in)}\hat{\tilde{X}}^\star_{(n)}\right)\right\} \tag{A.7}
$$

$$
\begin{aligned}
{}^{3}\mathbf{C}^{(8)} = \frac{1}{2A_0}\Bigg\{&\sum_i\sum_n\left(\zeta^\star_{(i)}\hat{\tilde{\mathbf{K}}}^\star_{(in)}\hat{\tilde{Y}}^\star_{(n)}\right)+\sum_j\sum_n\left(\hat{\tilde{Z}}^\star_{(j)}\vec{e}_3\cdot\tilde{\hat{\mathbf{K}}}^\star_{(in)}\hat{\tilde{Y}}^\star_{(n)}\right)-\ldots\\
&\tfrac{1}{2}\sum_i\sum_m\left(\zeta^\star_{(i)}\hat{\tilde{\mathbf{K}}}^\star_{(im)}\cdot\vec{e}_3\hat{\tilde{\mathbf{Y}}}^\star_{(m)}\right)-\tfrac{1}{2}\sum_j\sum_m\left(\hat{\tilde{Z}}^\star_{(j)}\vec{e}_3\cdot\tilde{\hat{\mathbf{K}}}^\star_{(im)}\cdot\vec{e}_3\hat{\tilde{\mathbf{Y}}}^\star\right)\Bigg\}
\end{aligned} \tag{A.8}
$$

$$
\begin{aligned}
{}^{2}\mathbf{C}^{(9)} = \frac{1}{4A_0}\Bigg\{&\sum_i\sum_n\left(\zeta^\star_{(i)}\hat{\tilde{\mathbf{K}}}^\star_{(in)}\zeta^\star_{(n)}\right)+\sum_j\sum_n\left(\hat{\tilde{Z}}^\star_{(j)}\vec{e}_3\cdot\tilde{\hat{\mathbf{K}}}^\star_{(in)}\zeta^\star_{(n)}\right)+\ldots\\
&\sum_i\sum_m\left(\zeta^\star_{(i)}\hat{\tilde{\mathbf{K}}}^\star_{(im)}\cdot\vec{e}_3\hat{\tilde{Z}}^\star_{(m)}\right)+\sum_j\sum_m\left(\hat{\tilde{Z}}^\star_{(j)}\vec{e}_3\cdot\tilde{\hat{\mathbf{K}}}^\star_{(im)}\cdot\vec{e}_3\hat{\tilde{Z}}^\star\right)\Bigg\}
\end{aligned} \tag{A.9}
$$

Bibliography

[1] T. Belytschko, W.K. Liu, and B. Moran. *Non-linear finite elemts for continua and structures.* Wiley, Chichester, 2000.

[2] N. Buannic and P. Cartraud. Higher-order effective modelling of periodic heterogeneous beams - part I: Asymptotic expansion method. *Int. J. of Solids and Structures*, 38:7139–7161, 2001.

[3] P. Cartraud and T. Messager. Computational homogenization of periodic beam-like structures. *Int. J. of Solids and Structures*, 43:686–696, 2006.

[4] J. Hohe and W. Becker. Effective stress-strain relations for two-dimensional cellular sandwich cores: Homogenization, material models, and properties. *Appl. Mech. Rev.*, 55:61–87, 2002.

[5] V.G. Kouznetsova. *Computational homogenization for multi-scale analysis of multi-phase materials.* PhD thesis, Eindhoven University of Technology, 2002.

[6] V.G. Kouznetsova, W.A.M. Brekelmans, and F.T.P. Baaijens. An approach to micro-macro modeling of heterogeneous materials. *Comput. Mech.*, 27:37–48, 2001.

[7] V.G. Kouznetsova, M.G.D. Geers, and W.A.M. Brekelmans. Multi-scale second-order computational homogenization of multi-phase materials: a nested finite element solution. *Comp. Methods Appl. Mech. Engrg.*, 193:5525–5550, 2004.

[8] T. Liu, Z.C. Deng, and T.J. Lu. Design optimization of truss-cored sandwiched with homogenization. *Int. J. of Solids and Structures*, 43:7891–7918, 2006.

[9] MSC.Software Corporation. *MSC.marc Volume B: Element library*, 2005 edition.

[10] T. Rabczuk, J.Y. Kim, E.Samaniego, and T. Belytschko. Homogenization of sandwich stuctures. *Int. J. Numer. Meth. Engng.*, 61:1009–1027, 2004.

[11] P.M. Suquet. Local and global aspects in the mathematical theoty of plasticity. *Plasticity Today: Modelling, Methods and Applications*, pages 279–310, 1985.